

University of Stockholm
Department of Physics



Stockholm
University

MASTER'S DEGREE THESIS

DELAY BETWEEN GRAVITATIONAL AND ELECTROMAGNETIC
WAVES DUE TO GRAVITATIONAL LENSING

Supervisor at Stockholm University
Prof. Edvard Mörtzell

Supervisor at Università degli studi di Padova
Prof. Sabino Matarrese

Candidate
Paolo Cremonese

Academic Year 2016/2017

Abstract

The study of gravitational waves will be of great importance in future cosmology, but we can already develop useful research right now, in order to fulfil useful achievements for future observations. Here, I study the arrival time difference, due to gravitational lensing, between gravitational and electromagnetic signals coming from the same source. The number of article in literature about lensed gravitational waves and multimessenger cosmology is growing with time, especially in the last years, but there is only one article with the same purpose, Takahashi, 2016, and it is a good starting point for my work. My thesis focuses on gravitational waves with much lower frequencies. Earth observatories for gravitational waves are not sensible in these frequency regime. These waves, therefore, are studied by pulsar timing arrays (PTAs). PTAs study the time of arrival of the signals from millisecond pulsars, which are the best clocks in the universe. With this method, PTAs will be capable of detecting gravitational waves with frequency up to $f \sim 10^{-8}/10^{-9}$ Hz.

A time delay is expected between gravitational and electromagnetic signals because of their large difference in frequency. Indeed, in the case of the electromagnetic light, we can study its bent path due to gravity in the geometrical optics regime, i.e. we can treat light propagation in terms of rays. For gravitational waves with low frequencies wave optics is needed, that is, integrating the ray optics study over the whole surface of the wave. For this reason, gravitational and electromagnetic signals are expected to behave differently passing near a mass and, therefore, their time of arrival will be different. In particular, the wavelength of the gravitational wave being very large ($\lambda \sim 1$ pc), it will "feel" the lens less, and pass almost unperturbed, with respect to light, that has a much shorter wavelength.

The sources of such large gravitational waves are super massive binary black-holes (SMBBHs). Their study is fundamental to understand what kind of signal we are looking for, and that is why the chapter about these systems is the longest in this thesis. The interesting part is the electromagnetic signal associated with such peculiar sources. It is expected to be unique and, there-

fore, "easily" recognizable and it should give different informations about the system, such as, for example, its period.

The final goal of the thesis is to understand the feasibility of such observations. Starting from different result and equations from literature, I show that, for next generation observatories, this feature will be observable with good precision, for a large range of sources. With current technologies, the task is harder, and only a lucky case could be actually observed.

Contents

Abstract	iii
1 Introduction	1
1.1 Gravitational Waves	2
1.1.1 GWs in empty space	3
1.1.2 Emission of GWs	4
1.2 Gravitational Lensing	7
1.2.1 Point mass	9
1.2.2 Singular Isothermal Sphere	12
1.3 Geometrical Optics <i>vs</i> Wave Optics	14
1.3.1 Geometrical Optics	15
1.3.2 Wave Optics	15
2 Gravitational Wave Detection	17
2.1 Pulsar	17
2.2 Pulsar Timing Array	19
2.2.1 Pulsar Timing Array Collaborations	21
2.2.2 Latest and future results	23
3 Super Massive Binary Black Holes	27
3.1 Characteristics of the emitted gravitational signal	28
3.2 Electromagnetic signal	31
3.2.1 Detectability of EM counterparts	36
3.2.2 Observation	40
4 Time delay	43
4.1 Calculate time delay	43
4.1.1 Lensed GWs	43
4.1.2 Lensed light	45
4.1.3 Time delay	45
4.2 Sensitivity of observations	47

5	Conclusions	53
5.1	Summary	53
5.2	Final results & discussion	54
5.3	Future works	56
A	About I and GWs	57
	Bibliography	59

Chapter 1

Introduction

The field of cosmology is incredibly wide and comprehend numerous and very different tasks. A great innovation will be brought, in large part of these subject, when we will be capable of study gravitational waves well enough. In the last years, the research and interest about gravitational waves has increased considerably. Almost two years ago (September 2015) the first direct observation of a gravitational wave was made by the two detectors of the Laser Interferometer Gravitational-Wave Observatory (LIGO), (Abbott, 2016). This observation opened a whole new field of study in astrophysics. As new observatories - such as VIRGO and Advanced VIRGO, in Italy, the Japanese groundbased interferometer KAGRA (the KAmioka GRAvitational wave detector), eLISA (the Evolved Laser Interferometer Space Antenna), and DECIGO (the DECI-hertz Interferometer Gravitational wave Observatory) - will be completed and begin operations, they will give us a new powerful instrument to study the universe. Moreover, another method is being developed and used to study gravitational signals with much lower frequency, the pulsar timing array. This method is taken into account for my work and it will be explained later on in this thesis.

In this work, I will study the arrival time differences, due to gravitational lensing, between gravitational waves and electromagnetic signals, emitted by one source at the same time or with known intrinsic time-delays. A first work on this topic has been developed by Takahashi, 2016. He studied the cases of two lens configurations (point mass and singular isothermal sphere lens) for monochromatic and chirp signals in a given range of wavelengths. He found that the lens imprints a characteristic modulation on a chirp waveform, so that one can be sure that the time delay is due to the lens; and that there will be a delay between gravitational and electromagnetic signal, due to the different wavelengths of the signals.

First of all, there are some basic fact we have to understand for what we are going to discuss. The main subjects are:

- 1.1 Gravitational Waves
- 1.2 Gravitational Lensing
- 1.3 Geometrical Optics & Wave Optics

1.1 Gravitational Waves

Gravitational waves (GWs) are tensor perturbations of the metric induced by a time variation of the second derivative of the quadrupole moment tensor of the energy density of the source.

Gravitational waves follow directly from the general theory of relativity. We can deduce their existence starting from Einstein equations. The complete¹ set of Einstein equations are

$$R_{\alpha\beta} - \frac{1}{2}Rg_{\alpha\beta} = \frac{8\pi G}{c^4}T_{\alpha\beta}, \quad (1.1)$$

where $g_{\alpha\beta}$ is the metric, $R_{\alpha\beta}$ is the Ricci tensor (contraction of the Riemann curvature $R^\gamma_{\alpha\theta\beta}$ with the metric $g_{\gamma\theta}$), R is the Ricci scalar (contraction of Ricci tensor with the metric) and $T_{\alpha\beta}$ is the energy-stress tensor. First, we use the weak field approximation, where we can rewrite $g_{\mu\nu}$ as

$$g_{\mu\nu} = \eta_{\mu\nu} + h_{\mu\nu}. \quad (1.2)$$

Here $\eta_{\mu\nu}$ is the Minkowski flat space-time metric and $h_{\mu\nu}$ is a small perturbation of the flat space-time, $h_{\mu\nu} \ll 1$. We can write Einstein equations in term of the metric $g_{\mu\nu}$ ², and simplify them if we consider a change in coordinates: $x'^\alpha = x^\alpha + \xi^\alpha(x)$, called *gauge transformation*, where $\xi^\alpha(x)$ is small. Using this change, we obtain a new metric $h'_{\alpha\beta} = h_{\alpha\beta} - \partial_\alpha\xi_\beta - \partial_\beta\xi_\alpha$. The point is, $\xi^\alpha(x)$ being arbitrary functions, we can set them in order to have³ $V_\alpha = \partial_\delta h_\alpha^\delta - \frac{1}{2}\partial_\alpha h_\gamma^\gamma = 0$, known as *Lorenz gauge*. In this case, the Lorenz gauge can be written in the simple form: $\partial_\beta\bar{h}^{\alpha\beta} = 0$, where $\bar{h}_{\alpha\beta} \equiv h_{\alpha\beta} - \frac{1}{2}\eta_{\alpha\beta}h$ is the trace-reverse perturbation. Substituting this perturbation in the Einstein tensor $G_{\alpha\beta} = R_{\alpha\beta} - \frac{1}{2}Rg_{\alpha\beta}$, using the Lorenz gauge yields

$$\square\bar{h}_{\alpha\beta} = -\frac{16\pi G}{c^4}T_{\alpha\beta}, \quad (1.3)$$

¹ We are not taking into account any cosmological constants or similar.

² I derived it here only for the case of empty space, paragraph 1.1.1.

³ We will see later, eq. (1.5), what is the reason of this choice.

where $\square \equiv \eta^{\alpha\beta} \frac{\partial^2}{\partial x^\alpha \partial x^\beta} = -\frac{\partial^2}{\partial t^2} + \nabla^2$ is the d'Alembert operator. This is the linearised Einstein equation for weak sources, and can be seen as a general gravitational wave equation, where the d'Alembertian is the wave operator and the energy-stress tensor $T_{\alpha\beta}$ is the source.

1.1.1 GWs in empty space

We infer the form of the waves in empty space, far away from any mass-energy source. We know that in vacuum, Einstein equations (1.1) are reduced to $R_{\mu\nu} = 0$. Rewriting the Ricci tensor in terms of the metric (1.2), we find $R_{\mu\nu} = (R_{\mu\nu})_0 + \delta R_{\mu\nu} = 0$ where $(R_{\mu\nu})_0$ is the Ricci tensor calculated in flat space-time, so it equals zero and therefore we are left with $\delta R_{\mu\nu} = 0$ ⁴. We now want to show explicitly $\delta R_{\mu\nu} = 0$ in terms of $h_{\mu\nu}(x)$. Using the expression for Ricci tensor in terms of the Christoffel symbols, and of this one in terms of the metric, we find

$$\delta R_{\alpha\beta} = \frac{1}{2} \left[-\square h_{\alpha\beta} + \partial_\alpha \left(\partial_\gamma h_\beta^\gamma - \frac{1}{2} \partial_\beta h_\gamma^\gamma \right) + \partial_\beta \left(\partial_\delta h_\alpha^\delta - \frac{1}{2} \partial_\alpha h_\gamma^\gamma \right) \right] = 0. \quad (1.4)$$

Defining $V_\alpha = \partial_\delta h_\alpha^\delta - \frac{1}{2} \partial_\alpha h_\gamma^\gamma$, we obtain

$$\delta R_{\alpha\beta} = \frac{1}{2} (-\square h_{\alpha\beta} + \partial_\alpha V_\beta + \partial_\beta V_\alpha). \quad (1.5)$$

We can further simplify this equation using the Lorenz gauge, and it will finally give us:

$$\square h_{\alpha\beta} = 0. \quad (1.6)$$

This is the gravitational wave equation in empty space.

A solution, $f(x)$, for this equation can be written, $f(x) = Ae^{ik^\mu x_\mu}$. It follows that $\square f(x) = -k^\mu k_\mu f(x) = 0$, from which we can infer that $k^\mu k_\mu = 0$. This means that $k^\mu = (|\vec{k}|, \vec{k})$ is a null four-vector and that the gravitational waves travel at the speed of light, since we are using the natural units, where $c = 1$. This is an important result for our discussion, because we just proved that if GWs and Electromagnetic (EM) waves are emitted at the same time, any arrival time differences between the signals is to be explained by some other cause, being their speed in vacuum the same. It is also true that massive gravity theories are developing in last years. In that case, the graviton being massive, the speed of GWs should be less than the speed of light. In this work, though, we consider the classic meaning of general relativity theory. A more general solution of the wave equation is $f(x) = \int d^3k a(\vec{k}) e^{ik^\mu x_\mu}$, given

⁴ This is a set of 10 linear, partial differential equation for $h_{\mu\nu}(x)$.

by the superposition of waves with different frequencies. In term of the metric, the solution is

$$h_{\alpha\beta}(x) = a_{\alpha\beta} e^{ik^\mu x_\mu}, \quad (1.7)$$

where $a_{\alpha\beta}$ is a constant, symmetric (0,2) tensor. Again, from the Lorenz gauge we can set $a_{0,\beta} = 0$ and $a_\beta^\beta = 0$. From the latter equation and $V_\alpha = 0$, we find $k^j a_{ij} = 0$. That shows that gravitational waves are transverse, as are EM waves.

In order to find an explicit solution to the wave equation, we simplify the problem and select spatial coordinates such that the wave is travelling in the z direction. Then $k^\mu = (\omega, 0, 0, k^3) = (\omega, 0, 0, \omega)$. Putting together all the conditions seen before will lead us to⁵:

$$h_{\alpha\beta} = \begin{pmatrix} 0 & 0 & 0 & 0 \\ 0 & a & b & 0 \\ 0 & b & -a & 0 \\ 0 & 0 & 0 & 0 \end{pmatrix} e^{i\omega(z-t)}. \quad (1.8)$$

It is straightforward to see that there are two polarizations of the waves. These are proportional to a or b , and are usually called the + (plus) and the \times (cross) polarization. The most general solution is given by the superposition of waves with different ω , different direction of propagation and different amplitudes for the two kinds of polarization.

1.1.2 Emission of GWs

We now want to study the generation of gravitational waves by matter sources. Eq. (1.3) can be seen as a general equation of the type,

$$-\frac{\partial^2 f(x)}{\partial t^2} + \nabla^2 f(x) = j(x), \quad (1.9)$$

with $f(x)$ being the metric and $j(x)$ the source. The solution to this equation can be achieved through the Green function $g(t, r)$, first considering the source as a δ -function located in a definite point in the space-time. The δ -function being hard to deal with, we take eq. (1.9), integrate both sides of it over a small volume of radius r , and make r go to zero. We then find,

$$\lim_{r \rightarrow 0} \int_r d^3 x \square g(x^\mu) = \lim_{r \rightarrow 0} \int_r d^3 x \delta(t) \delta^{(3)}(\vec{x}) = \delta(t), \quad (1.10)$$

⁵ This choice of coordinates in which the transverse and traceless condition are represented explicitly is called *transverse-traceless gauge*, or TT-gauge.

where the part involving the time ($\partial^2 g / \partial t^2$) goes to zero as $r \rightarrow 0$ ⁶. Now, substituting $g(t, r) = O(t-r)/r$, that is, the retarded solution of the homogeneous part of eq. (1.9), with $O(\cdot)$ a general function, we find $-4\pi O(t) = \delta(t)$ and the solution $g(t, r)$ will be

$$g(t, r) = -\frac{\delta(t-r)}{4\pi r}. \quad (1.11)$$

This solution is for a δ -function source at the origin and an outgoing wave. Generalizing the result, which means taking into account that the source is extended and not just a point, $f(t, \vec{x}) = -\frac{1}{4\pi} \int d^3x' \frac{[j(t', \vec{x}')]_{\text{ret}}}{|\vec{x} - \vec{x}'|}$, where $[\cdot]_{\text{ret}}$ means that the argument should be evaluated at retarded time, the solution⁷ becomes

$$\bar{h}^{\alpha\beta}(t, \vec{x}) = 4 \int d^3x' \frac{[T^{\alpha\beta}(t', \vec{x}')]_{\text{ret}}}{|\vec{x} - \vec{x}'|} \quad (1.12)$$

for $\bar{h}^{\alpha\beta}$ with the source $-16\pi T^{\alpha\beta}$. Far away from the source, the solution will be⁸

$$\bar{h}^{\alpha\beta}(t, \vec{x}) \xrightarrow{r \rightarrow \infty} \frac{4}{r} \int d^3x' [T^{\alpha\beta}(t-r, \vec{x}')]_{\text{ret}}. \quad (1.13)$$

Now, if we use the conservation law for $T^{\alpha\beta}$, and assume that the source moves with non relativistic velocities, we finally find⁹:

$$\bar{h}^{ij}(t, \vec{x}) \xrightarrow{r \rightarrow \infty} \frac{2G}{r} \ddot{I}^{ij}(t-r), \quad (1.14)$$

where $I^{ij}(t) \equiv \int d^3x x^i x^j \rho(t, \vec{x})$ is the quadrupole moment tensor of the energy density of the source.

Binary stars

A starting point for understanding the work by Takahashi, 2016 - where they studied gravitational waves that may come, among other sources, from

⁶ $g \rightarrow \infty$ for $r \rightarrow 0$ but the volume element is decreasing as $4\pi r^2$.

⁷ $j(t', \vec{x}')$ comes from $\square f(x) = j(x)$, $j(x) \equiv \delta(t)\delta(x)\delta(y)\delta(z)$ represents the source. The prime is to refer at the retarded (or the source) quantities.

⁸ The asymptotic solution far from a source, whose size is much smaller than the wavelength, is

$$f(t, \vec{x}) \xrightarrow{r \rightarrow \infty} -\frac{1}{4\pi r} \int d^3x' j(t-r, \vec{x}').$$

⁹ For more details, see Appendix A.

binary neutron star (NS) mergers, NS–BH mergers, or BH–BH binaries - is to consider a system composed by two stars. Therefore, we consider two stars of equal mass M , whose motion is in the x - y plane, orbiting around the common barycentre (see Figure 1.1). Then, we write,

$$x(t) = R \cos(\Omega t), \quad y(t) = R \sin(\Omega t), \quad z(t) = 0, \quad (1.15)$$

where R is the radius of the orbit, and Ω the orbital frequency of the stars. Therefore, the components of the quadrupole momentum are

$$I^{xx} = 2MR^2 \cos^2(\Omega t) = MR^2[1 + \cos(2\Omega t)] \quad (1.16a)$$

$$I^{xy} = 2MR^2 \cos(\Omega t) \sin(\Omega t) = MR^2[\sin(2\Omega t)] \quad (1.16b)$$

$$I^{yy} = 2MR^2 \sin^2(\Omega t) = MR^2[1 - \cos(2\Omega t)] \quad (1.16c)$$

so, considering equation (1.14), we end up with

$$\bar{h}^{ij} \xrightarrow{r \rightarrow \infty} -\frac{8G\Omega^2 MR^2}{r} \begin{pmatrix} \cos[2\Omega(t-r)] & \sin[2\Omega(t-r)] & 0 \\ \sin[2\Omega(t-r)] & -\cos[2\Omega(t-r)] & 0 \\ 0 & 0 & 0 \end{pmatrix}. \quad (1.17)$$

The frequency of the emitted radiation is thus twice the orbital frequency, Ω .

Generalizing this result to any binary inclination with respect to the line of sight, and binary with different mass stars, gives

$$\begin{pmatrix} h_+(t) \\ h_x(t) \end{pmatrix} = \frac{1}{r} \frac{4G\mu\Omega^2 R^2}{c^4} \begin{pmatrix} (1 + \cos^2 \iota) \cos(2\Omega(t)) \\ \cos \iota \sin(2\Omega(t)) \end{pmatrix}, \quad (1.18)$$

where $\mu = m_1 m_2 / (m_1 + m_2)$, and ι is the angle between the rotation axis of the binary and the line of sight.

About GW in Takahashi, 2016

Takahashi considers gravitational waves with wavelengths large enough to be in the wave optics regime^a, with frequencies of about 10 Hz to 1 kHz. There are also cases, for example when the sources responsible for the signals are merging (see Fig. 4 in the paper), where the wavelength shortens enough to be close to the geometrical optics regime. In that case, multiple images form and we see a modulation (interference pattern) of the total wave. In this thesis, I study gravitational waves with larger wavelengths, described by wave optics. As we will see, the limit between geometrical and wave optics depends also on the lens mass. I consider galaxies as lenses, i.e. with mass $\approx 10^{11} M_\odot$. The frequency range in this case is between 10^{-6} and 10^{-8} Hz, corresponding to a period between 10 days and 1 year.

^a See chapter 1.3.

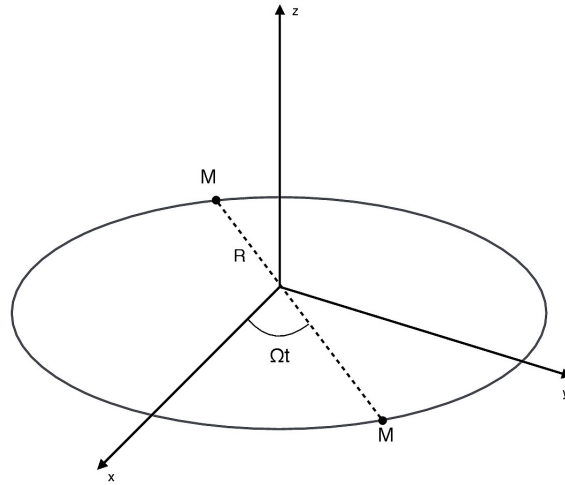


Figure 1.1: Binary star system.

1.2 Gravitational Lensing

From general relativity, we know that light passing close to a mass (e.g. a star, a galaxy or a galaxy cluster), is bent by the gravitational field of the mass, that is, the lens. Therefore, light does not follow a "straight" line but changes direction, as when it flows from a medium to another with different refraction index. In this case, the refraction index, n , is given by the potential:

$$n = 1 - \frac{2}{c^2}\phi, \quad (1.19)$$

where ϕ is the Newtonian potential. Because of this, we can deduce that light will travel slower near the source and will have a delay with respect to the light travelling in a flat space-time. The delay can be calculated using the *Shapiro time delay*, equation (1.20).

Shapiro time delay General relativity tells us that a clock slows down, as the gravitational field which the clock is immersed in increases. For this reason, c being constant, if time slows down, then light has a delay with respect to light that passes through flat space-time (or through a weaker gravitational field). That is because if light takes 1 second to travel $3 \cdot 10^8$ m and 1 second "lasts longer" in a stronger gravitational field, then it is as if light is slowed down. We can quantify this delay by the equation:

$$\Delta t = \int_{\text{source}}^{\text{observer}} \frac{2}{c^3} |\phi| dl \quad (1.20)$$

where ϕ is the potential of the gravitational field.

Before going on studying two specific lens configurations, let us define two more quantities that are useful for later discussions.

Effective lensing potential We define an *effective lensing potential*, ψ , such that $\vec{\nabla}_\theta \psi = \vec{\alpha}$, where $\vec{\alpha}$ is the deflection angle defined in eq. (1.26), and $\nabla_\theta^2 \psi = 2 \frac{\Sigma(\vec{\theta})}{\Sigma_{cr}} \equiv 2\kappa(\vec{\theta})$, where $\kappa(\vec{\theta})$ is called the *convergence*. The local properties of the lens mapping are described by the Jacobian matrix

$$\mathcal{A} \equiv \frac{\partial \vec{\beta}}{\partial \vec{\theta}} = \mathcal{M}^{-1}, \quad (1.21)$$

where \mathcal{M} is the magnification tensor. Therefore the magnification will be:

$$\mu = \det \mathcal{M} = \frac{1}{\det \mathcal{A}} = \frac{1}{[(1 - \kappa)^2 - \gamma^2]}. \quad (1.22)$$

Time delay function The time delay function describes the time difference between the arrival time of light that passes close to a lens and a light ray that travels in a flat space-time. The function is

$$t(\vec{\theta}, \vec{\beta}) = \frac{1 + z_d}{c} \frac{D_d D_s}{D_{ds}} \left[\overbrace{\frac{1}{2}(\vec{\theta} - \vec{\beta})^2}^{\propto t_{\text{geom}}} - \overbrace{\psi(\vec{\theta})}^{\propto t_{\text{grav}}} \right] = t_{\text{geom}} + t_{\text{grav}}. \quad (1.23)$$

t_{grav} is the Shapiro time delay, mentioned previously. t_{geom} is due to the extra path of the light with respect to the unlensed case. Take for example Figure 1.4: the real path of the light (S-A-O) is clearly longer than the unlensed one (S-O). One could argue that, near the lens, the space-time being curved, the path should be longer. That, though, is taken into account by the *Shapiro time delay*. Furthermore, that is also why t_{grav} has a maximum in the direction of the source, while t_{geom} has a minimum in the direction of the lens, as shown in Figure 1.2.

Now, we know from eq. (1.27) that¹⁰

$$\vec{\nabla}_\theta \left[\frac{1}{2}(\vec{\theta} - \vec{\beta})^2 - \psi \right] = 0. \quad (1.24)$$

Therefore, according to Fermat's principle stating that rays of light traverse the path of stationary travel time with respect to variations of the path, we get an image when the condition $\vec{\nabla}_\theta t(\vec{\theta}) = 0$ is satisfied, as seen from Figure 1.2.

¹⁰ This comes from $\vec{\beta} = \vec{\theta} - \vec{\alpha}(\vec{\theta}) \Rightarrow (\vec{\theta} - \vec{\beta}) - \vec{\alpha}(\vec{\theta}) = 0 \Rightarrow (\vec{\theta} - \vec{\beta}) - \vec{\nabla}_\theta \psi = 0$

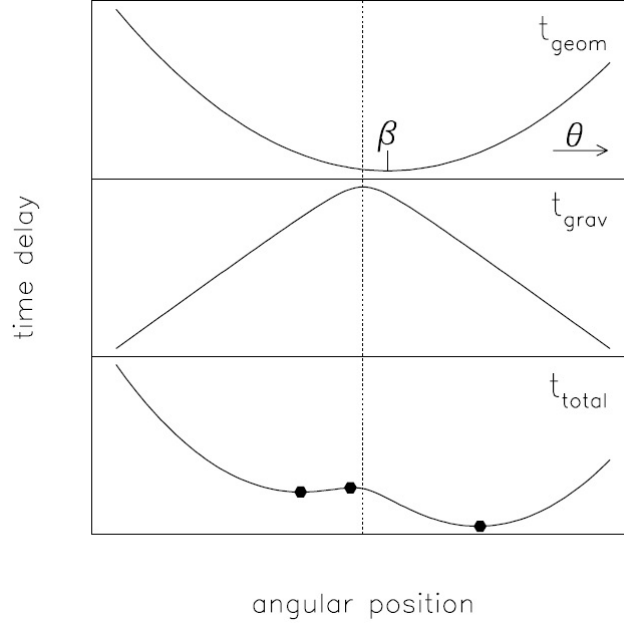


Figure 1.2: Time delay. The top panel shows t_{geom} . The delay is centred on the source and it is greater as the position of the image (θ) "get away" from the source. The medium panel is t_{grav} and it is greater as the light pass closer to the lens. For more information see paragraph *Time delay function* (1.2). The bottom panel is the combination of the two above. Figure from Narayan and Bartelmann, 1996.

1.2.1 Point mass

Assuming that the lens is a point mass, its potential is:

$$\phi(b, z) = -\frac{GM}{(b^2 + z^2)^{1/2}}, \quad (1.25)$$

where b is the impact parameter of the unperturbed light, and z indicates the direction along the unperturbed light path, with the origin A in the point closest to the lens (see Figure 1.3). The deflection angle is given by

$$\hat{\alpha} = \frac{2}{c^2} \int_{-\infty}^{+\infty} \nabla_{\perp}^2 \phi dz = \frac{4GM(\xi)}{c^2 \xi}, \quad (1.26)$$

where the last equation is valid for circularly symmetric lenses. In the case of a point mass lens, $\hat{\alpha} = \frac{4GM}{c^2 b} \equiv \frac{2R_s}{b}$. As seen from Figure 1.4, keeping in mind that all the angles involved are small and the angles in the figure are

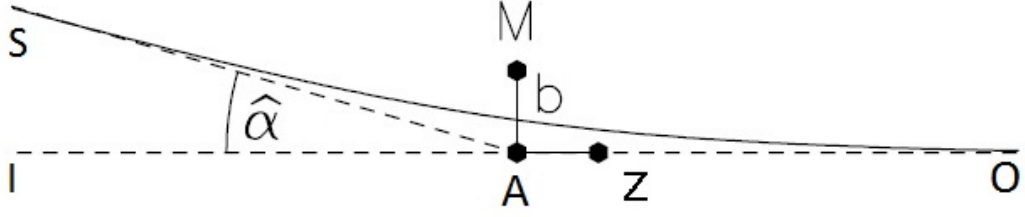


Figure 1.3: A gravitational lens configuration. S is the source, M the lens and O the observer. I is the position of the source as seen from the observer. Figure from Narayan and Bartelmann, 1996.

exaggerated for clarity, we can write $\theta D_s = \beta D_S - \hat{\alpha} D_{ds}$. In this way, we can relate the position of the source and the image with

$$\vec{\beta} = \vec{\theta} - \vec{\alpha}(\vec{\theta}) = \theta - \frac{\theta_E^2}{\theta}, \quad (1.27)$$

where $\vec{\alpha} = \frac{D_{ds}}{D_s} \hat{\alpha}$ and θ_E is the Einstein radius, defined as follows. Considering a circularly symmetric lens with an arbitrary mass profile, we have:

$$\beta(\theta) = \theta - \alpha(\theta) \quad (1.28)$$

and, since $\vec{\alpha} = \frac{D_{ds}}{D_s} \hat{\alpha} = \frac{D_{ds}}{D_s} \frac{4GM\theta}{c^2\theta}$, where D_{ds}, D_d and D_s are shown in Figure 1.4,

$$\beta(\theta) = \theta - \frac{D_{ds}}{D_d D_s} \frac{4GM(\theta)}{c^2\theta}. \quad (1.29)$$

Because of the rotational symmetry of the lens, if the source is exactly behind the lens, as seen from an observer far away from the lens and the source, then $\beta = 0$ and the image would be a ring with a radius given by the Einstein radius

$$\theta_E = \left[\frac{4GM}{c^2} \frac{D_{ds}}{D_d D_s} \right]^{1/2}. \quad (1.30)$$

The solutions to equation (1.27) for θ are

$$\theta_{\pm} = \frac{1}{2} \left(\beta \pm \sqrt{\beta^2 + 4\theta_E^2} \right). \quad (1.31)$$

Gravitational lensing changes the apparent shape of the image while preserving surface brightness, so the total flux of the source changes. This can be understood thinking about a magnifying glass. When we look at a screen through a magnifying glass it appears brighter, but, obviously, the brightness

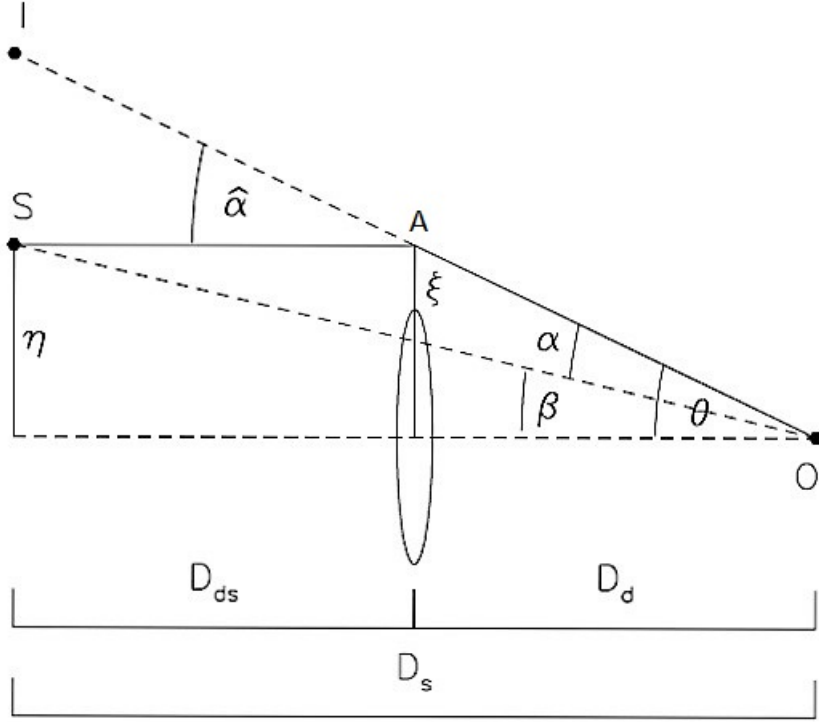


Figure 1.4: Gravitational lens system. S is the source and O the observer. The angular diameter distances between observer and lens, lens and source, and observer and source are D_d , D_{ds} , and D_s , respectively. I is the position of the source as seen from the observer. Figure from Narayan and Bartelmann, 1996.

of the screen itself does not change. The change in flux is quantified by the magnification and in the case of circularly symmetric lens, it is $\mu = \frac{\theta}{\beta} \frac{d\theta}{d\beta}$. In this equation, in the case of a point mass lens, we can use equation (1.27) for β so the magnification will be:

$$\mu_{\pm} = \left[1 - \left(\frac{\theta_E}{\theta} \right)^4 \right]^{-1}. \quad (1.32)$$

From this equation we can see that for $\theta \rightarrow \theta_E$, $\mu \rightarrow \infty$. That is not a problem because in a realistic case the source is never a perfect point and we need to take into account the wave optics approximation. This will change the equation, giving a finite μ .

1.2.2 Singular Isothermal Sphere

A slightly more complicated lens model is the *singular isothermal sphere* (SIS). This is usually used when the lens is a galaxy, or a cluster of galaxies. In my work, it is more likely that the lens is a galaxy than a cluster of galaxies. In this model, the stars, which compose the galaxy, are assumed to behave like particle of an ideal gas. Then, combining the equation of state of the stars, $p = \frac{\rho kT}{m}$, and the equations of hydrostatic equilibrium,

$$\frac{p'}{\rho} = -\frac{GM(r)}{r^2}, \quad (1.33a)$$

$$M'(r) = 4\pi r^2 \rho, \quad (1.33b)$$

where a prime denotes a derivative with respect to r , assuming that the gas composing the lens is isothermal (i.e., T , in the equation of state, is constant) we get a *singular isothermal sphere* mass distribution:

$$\rho(r) = \frac{\sigma_v^2}{2\pi G} \frac{1}{r^2}, \quad (1.34)$$

where σ_v is the one-dimensional velocity dispersion of the stars, in this case, constant¹¹ across the galaxy. Usually, most of the light deflection occurs in a region of the order of the distance of the closest point of the light path (A in Figure 1.4) to the lens. Most of the time, this distance is small compared to lens-source and observer-lens distances. Therefore, the lens can be considered thin and, projecting the density along the line-of-sight, we obtain the surface mass density,

$$\Sigma(\xi) = \frac{\sigma_v^2}{2G} \frac{1}{\xi}. \quad (1.35)$$

It follows that the projected mass within ξ is given by

$$M(\xi) = 2\pi \int_0^\xi \Sigma(\xi') \xi' d\xi'. \quad (1.36)$$

From eq. (1.26), (1.35), and (1.36), we evaluate the deflection angle in the source plane, that is $\hat{\alpha} = 4\pi \frac{\sigma_v^2}{c^2}$.

We have multiple images when the source lies within the Einstein radius. In this case we have two solutions: $\theta_\pm = \beta \pm \theta_E$. The magnification is

$$\mu_\pm = \frac{\theta_\pm}{\beta} = 1 \pm \frac{\theta_E}{\beta} = \left(1 \mp \frac{\theta_E}{\theta_\pm}\right)^{-1}. \quad (1.37)$$

¹¹ Indeed, we have $m\sigma_v^2 = kT$, and, since T is constant, so is σ_v .

<i>Characteristics</i> →	Effective Lensing	Deflection Angle
<i>Lens model</i> ↓	Potential $\psi(\theta)$	$\alpha(\theta)$
Point mass	$\frac{D_{ds}}{D_s D_d} \frac{4GM}{c^2} \ln \theta $	$\frac{D_{ds}}{D_s D_d} \frac{4GM}{c^2 \theta }$
Sis	$\frac{D_{ds}}{D_s} \frac{4\pi\sigma^2}{c^2} \theta $	$\frac{D_{ds}}{D_s} \frac{4\pi\sigma^2}{c^2}$

Table 1.1: In this table we can see the effective lensing potential $\psi(\theta)$ and the deflection angle $\alpha(\theta)$ for both a point mass and a singular isothermal sphere lens.

About Gravitational Lensing in Takahashi, 2016

In the paper by Takahashi, gravitational lensing is studied both for point masses and SIS lenses. There is a clarification, though, to be done about the time delay appearing in the article. The time delay for gravitational lensing is defined with respect to the unlensed case and given by (see eq. 1.23):

$$\Delta t \propto \left[\frac{1}{2} (\vec{\theta} - \vec{\beta})^2 - \psi(\vec{\theta}) \right]. \quad (1.38)$$

Usually, it is defined in order to have $\Delta t = 0$ for the unlensed case, $\Delta t > 0$ when the lensed signal arrives after the unlensed one and vice versa for $\Delta t < 0$. The latter case is rather unusual because it is due to rare situations, like the presence of exotic matter or of an under dense region along the path of the signal. Nonetheless, in the paper we find several time delays whose value is negative, but this is not a problem. In order to respect the definition above, the potential of the lens must be normalized, i.e. its value at infinity must be zero. That is not the case in the paper, because none of the potentials are normalized. The potential used in the paper can be seen in Table 1.1. Furthermore, for the *singular isothermal sphere* lens, one can never normalize the potential to zero at infinity since the mass diverges. Anyway, this is not a problem if one keeps just in mind that the definition above are no longer valid (i.e. $\Delta t < 0$ does not mean that the lensed signal arrives before the unlensed one). Besides, what we actually measure is not the delay with respect to the unlensed case (it would be impossible to measure), but the different arrival time for different images, different source positions or different frequencies. Therefore, again, negative time delay are not a problem.

1.3 Geometrical Optics vs Wave Optics

Geometrical (or ray) optics and wave (or physics) optics are two ways to study the propagation of waves, like EM waves but also, in our case, gravitational waves. Further below there is a simple definition of those approaches, but first we need to understand when to use one and when the other. There are different ways to define the passage between the two "approximations":

- Takahashi and Nakamura, 2003 say "in the gravitational lensing of gravitational waves, the wave optics should be used instead of the geometrical optics when the wavelength λ of the gravitational waves is longer than the Schwarzschild radius of the lens mass" (see also Nakamura and Deguchi, 1999)
- in Schneider, Ehlers, and Falco, 1992 we find that "when the wavelength is larger than the path difference between the multiple images, the geometrical optics approximation breaks down".

Actually, we can see that those definition are the same. That is because the second definition can be written as: if $\lambda > \Delta D_{\text{im}}$, where λ is the wavelength and ΔD_{im} is the difference between the path of the images, then we should use wave optics. ΔD_{im} is of course proportional to the time difference ΔT_{im} of the images, in particular: $\Delta T_{\text{im}} = \Delta D_{\text{im}}/c$. It is also true that $\Delta T_{\text{im}} \sim \frac{D_d \alpha^2}{c}$ and $\alpha \sim \frac{d}{D_d}$, where d is the distance between two images. Therefore we have:

$$\Delta D_{\text{im}} = \Delta T_{\text{im}} \cdot c \sim \frac{D_d \alpha^2}{c} c \sim d \alpha = \frac{2d}{b} R_s \sim R_s \quad (1.39)$$

Where we also used the definition of α as written right below eq. (1.26). From eq. (1.39) we can infer that $\lambda > \Delta D_{\text{im}}$ is the same as $\lambda > R_s$.

In the article by Takahashi, 2016, the condition is also seen differently. That is, let us figure out what is the value of the mass of a lens that divides geometrical from wave optics, with respect to the wavelength of the gravitational wave (for the EM waves, we are always in the geometrical optics approximation). Therefore,

$$\lambda \geq R_s = \frac{2GM}{c^2} \approx \frac{GM}{c^2} \Rightarrow M \leq \frac{c^2}{G} \lambda \simeq 6,742 \cdot 10^{-4} M_\odot \left(\frac{\lambda}{\text{m}} \right) \approx 10^5 M_\odot \left(\frac{f}{\text{Hz}} \right)^{-1} \quad (1.40)$$

and

$$M \leq 10^5 M_\odot \left(\frac{f}{\text{Hz}} \right)^{-1}. \quad (1.41)$$

For example, for a solar mass lens, the "border" wavelength would be $\lambda \approx 3$ km $\Rightarrow \nu \approx 10^5$ Hz. For a galaxy, $M = 10^{11} M_{\odot}$, $\lambda \approx 1.47 \cdot 10^{14}$ m $\Rightarrow \nu \approx 10^{-6}$ Hz. This means that for larger λ (or smaller ν) than the values just found, wave optics must be used. For $\nu \approx 10^{-8}$ Hz $\Rightarrow M < 10^{13} M_{\odot}$. Which means that, for lenses with mass smaller than $10^{13} M_{\odot}$, wave optics must be used. These examples are not casual, indeed $M = 10^{11} M_{\odot}$ is the average mass of a galaxy that could act as lens for my study, while $\nu \approx 10^{-8}$ Hz is a typical GW frequency measured by Pulsar Timing Arrays (PTAs, see chapter 2.2). We can see that, for the study of this thesis, wave optics must be applied to study GWs.

1.3.1 Geometrical Optics

Geometrical optics, or ray optics, describes light propagation in terms of rays. The ray in geometric optics is an abstraction, or instrument, useful in approximating the paths along which light propagates in certain classes of circumstances.

The simplifying assumptions of geometrical optics include that light rays: i) propagate in rectilinear paths as they travel in a homogeneous medium; ii) bend, and in particular circumstances may split in two, at the interface between two dissimilar media; iii) follow curved paths in a medium in which the refractive index changes may be absorbed or reflected.

Geometrical optics does not account for certain optical effects such as diffraction and interference. This simplification is useful in practice; it is an excellent approximation when the wavelength is small compared to the size of structures with which the light interacts. The techniques are particularly useful in describing geometrical aspects of imaging, including optical aberrations.

1.3.2 Wave Optics

Wave (or physical) optics is the name of an approximation commonly used in optics, electrical engineering and applied physics. In this context, it is an intermediate method between geometric optics, which ignores wave effects, and full wave electromagnetism, which is a precise theory. The word "physical" means that it is more physical than geometric or ray optics and not that it is an exact physical theory. This approximation consists of using ray optics to estimate the field on a surface and then integrating that field over the surface to calculate the transmitted or scattered field. This resembles the Born approximation, in that the details of the problem are treated as a perturbation.

In optics, it is a standard way of estimating diffraction effects. In radio, this

approximation is used to estimate some effects that resemble optical effects. It models several interference, diffraction and polarization effects, but not the dependence of diffraction on polarization. Since it is a high-frequency approximation, it is often more accurate in optics than for radio. In optics, it typically consists of integrating ray-estimated field over a lens, mirror or aperture to calculate the transmitted or scattered field.

Chapter 2

Gravitational Wave Detection

As mentioned in the introduction, several detectors for gravitational waves are under construction, and a couple of them are already in use. Most of them work through laser interferometry (e.g., LIGO, VIRGO, eLISA). The frequency range for those detectors is between 10^{-5} to 10^4 Hz (see Figure 2.1). As said before, Takahashi, 2016 worked in this range. In this work, I will study gravitational waves whose wavelength is much larger, of the order of 10^{-8} Hz (= 10 nHz, that is $\lambda \sim 1$ pc or period $T \sim 1$ year), mostly coming from super massive binary black-holes (SMBBHs). Therefore, we need different detectors.

The great thing about astronomy is that, to accomplish its research, since most of the time it can not make laboratories experiments, it is forced to use what the universe offers. In this case, pulsars.

2.1 Pulsar

A pulsar is a neutron star in one of the latest stages in the life of a star. It is a very compact object, its mass is of the order of $1 M_{\odot}$ while having a radius of ~ 10 Km. It also has a very intense magnetic field, $B \sim 10^{12}$ G (while a star usually has $B \sim 10^{2-3}$ G). Considering the pulsar as an advanced stage of a star, the value of the magnetic field comes from the conservation of magnetic flux: $B_i R_i^2 = B_f R_f^2$, where f corresponds to the pulsar and i to its progenitor. Therefore,

$$B_f = B_i \left(\frac{R_i}{R_f} \right)^2 \approx 100 \left(\frac{10^6}{10} \right)^2 \approx 10^{12} G. \quad (2.1)$$

The most important characteristics of these objects are their beamed emission and their short rotation period. Simplifying, the latter can be deduced as

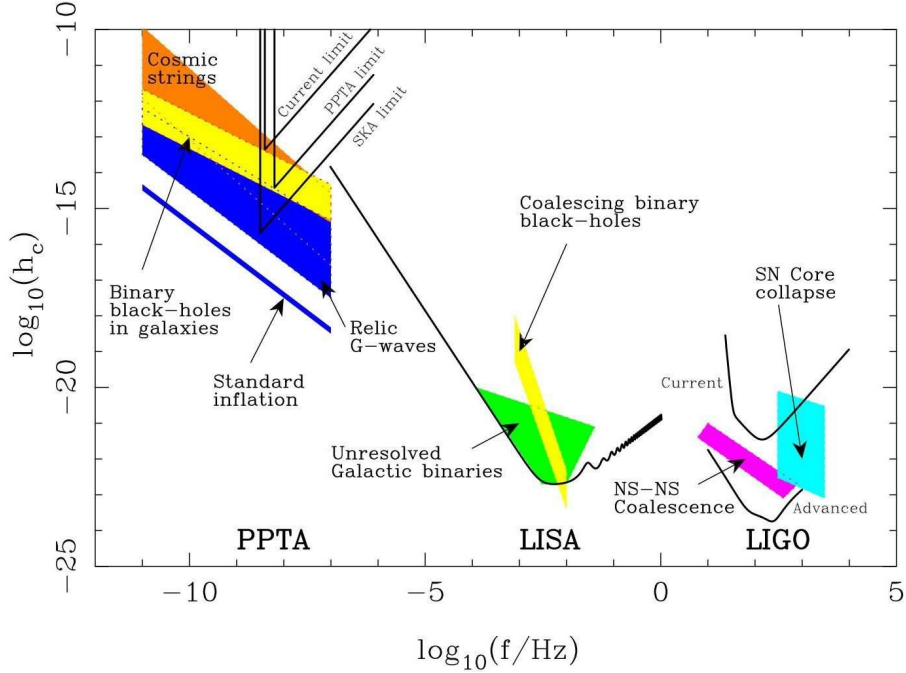


Figure 2.1: Spectrum of potentially detectable GW sources and sensitivity curves for PTA systems, the space-based laser interferometer LISA and the ground-based laser interferometer LIGO. Figure from Manchester, 2010.

in eq. (2.1), recalling the conservation of angular momentum, giving a period of the order of seconds¹. The fast rotation combined with the beamed emission give the peculiar characteristic of the observed pulse. The wavelength of the emission could vary over a large range of wavelengths, but in particular they emit in the radio range. Of course, a pulsar can only be detected if, at any time of the rotation, the beamed emission is pointed to the earth.

A part from usual pulsars, which have periods between 0.1 and 5 seconds, there is another type of pulsar, the milliseconds pulsars (MSPs). These have periods of milliseconds (from 2 to 50 ms), and are also called recycled pulsar. This is because they were old silent pulsars with long periods which, thanks to an evolving companion star, gained material and, most of all, angular mo-

¹ Actually, doing the calculation, the period is $\sim 10^{-5}$ s. Then, because of the huge magnetic field, the star is slowed down quickly.

mentum. At the same time, this process reduces the effective magnetic field of the pulsar, which is responsible for the emission. Nonetheless, thanks to its big spin-rate, the emission beam is reactivated.

Because of their short period, their compactness and small magnetic field² that give a high stability to the star and to its period, and their beamed emission, MSPs are extremely precise clocks and, for this, are useful objects for astronomy. In my case, for the detection of GWs.

2.2 Pulsar Timing Array

The technique used to detect GW, through MSPs, is called Pulsar Timing Array (PTA). It consists of monitoring the observed beam frequency of several MSPs over a long period of time. The aim is to reconstruct the pulse of the star as precisely as possible. The rotational phase of the pulsar, at time t , is

$$\phi(t) = \phi(t_0) + f(t - t_0) + \frac{1}{2}\dot{f}(t - t_0)^2 + \dots, \quad (2.2)$$

where $f = d\phi/dt$ is the rotation frequency, and \dot{f} is the first time derivative of f , and both are the unknowns of the problem. What is done, in practice, is to take the time of arrival (TOA) of a pulsar as measured at the telescope and to convert it in an inertial reference frame with respect to the pulsar. Usually, the rest frame is the barycentre of the solar system. Therefore,

$$t = t_{topo} - t_{topo,0} + \Delta_{clock} - \Delta_{DM} + \Delta_{R\odot} + \Delta_{E\odot} + \Delta_{S\odot} + \Delta_R + \Delta_E + \Delta_S, \quad (2.3)$$

where $topo$ indicates the topocentric frame (i.e. the observer frame), Δ_{clock} accounts for differences between the observatory clock and a terrestrial time standard, Δ_{DM} (where DM stays for dispersion measure) is the correction due to the inter stellar medium (ISM), $\Delta_{R,E,S}$ are respectively Römer delay that accounts for light travel time across an orbit, Einstein delay, which takes into account time dilation due to orbital motion and the gravity of other bodies, and Shapiro delay. The \odot indicates quantities arising from Sun and other bodies in the solar system, while the others are referred to the Earth. It is good to remind that some of these quantities are time dependent, like for example Δ_{DM} . Therefore, this work has to be really precise and continuous. Once it is done, we can build a *timing model*, to reconstruct the rotational phase of the pulsar [eq. (2.2)], at any given time. At this point, the observed TOA is compared to the prediction made by the model just presented. The

² The main cause of the slowdown, in the pulsar, is the strong magnetic field.

difference between these two quantities is called *timing residual*. This is usually different from zero, despite the correction that have been made, and it is due to different noises. The noise is called *red* or *white*, depending on whether its power spectral density rises with frequency or stay flat, respectively. *White noise* is due to radiometer noise, pulse jitter, and interstellar oscillation, while timing noise, dispersion measure (DM) variation, and GW cause *red noise*. Most of these noises can be reduced, or even deleted, increasing observing and integration time, increasing radio bandwidth, observing with larger telescopes, and by using low-noise receivers and amplifiers³. Assuming all the correction have been done correctly and all noise been reduced as much as possible, what is left, in term of *timing residual*, is possibly due to GWs. As in laser interferometry detectors, the wave passing between the pulsar and the Earth, warps space-time, inducing a modulation in the TOA with respect to the model⁴.

The main reasons to use a PTA are that one (i) can increase signal-to-noise ratio of the GW in the *timing residual*, and (ii) compare *timing residual* from different pulsars to discriminate between GW signal and other noises. Indeed, because of the quadripolar nature of GWs, the signal we are looking for contains unique characteristics. In particular, as seen in Figure 2.2, it gives a unique correlation between *timing residual* from different pulsars, distributed in the sky. The figure shows the correlation, which depends only on the angle separation between the pulsars, for a stochastic and isotropic signal of GW, i.e. a Gravitational Wave Background (GWB). The trend of the plot will be clear when, in chapter 3.1, I will explain how the *time residual* takes place from GWs. In particular, eq. (3.3), will show how this *time residual* depends on the relative position of source-pulsar-Earth. Therefore, in the case of an isotropic background radiation, the value will depend only on the relative positions of the pulsars. The maximum correlation is 0.5 and not 1 because the pulsar terms, which will be presented in chapter 3.1, are never correlated. For a single detection, the problem is not so simple, and other variables are to be considered, making a single detection less probable than a GWB detection⁵.

On the other hand, an error in the transformation between the observatory clock and a terrestrial time standard [Δ_{clock} in eq. (2.3)] would have a monopolar signature, and an error in $\Delta_{S\odot}$ would have a dipolar signature. Therefore, a pulsar timing array is needed not just to monitor many different pulsars and to have more data, but also because of this unique correlation.

³ See Manchester, 2010 for more detail about noises.

⁴ For further explanation see chapter 3.1.

⁵ For further investigation see Rosado, Sesana, and Gair, 2015 and chapter 3.1.

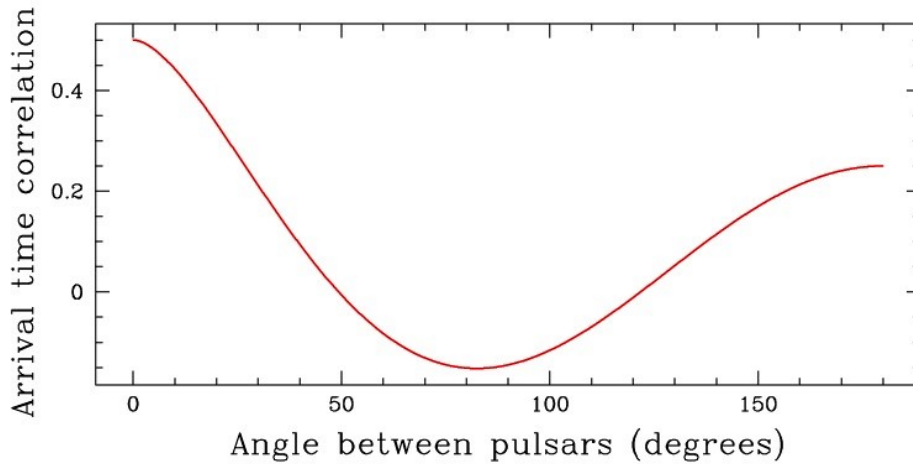


Figure 2.2: The Hellings-Downs curve showing the expected angular correlation between pulsar timing residuals as a function of angular separation. It was first explained by Hellings and Downs, 1983. Figure from Lynch, 2015.

Besides, by studying many pulsars, it will be possible to reconstruct the position in the sky of the source. For example, Anholm et al., 2009, through simulations, examined how well the PPTA (Parkes Pulsar Timing Array, see next paragraph) should constrain the position of a GW source, see Figure 2.3.

2.2.1 Pulsar Timing Array Collaborations

There are currently three major PTA collaborations.

- The European Pulsar Timing Array⁶ (EPTA) uses five telescopes to monitor northern sky pulsars. The 100 m Effelsberg Radio Telescope in Germany, the 76 m Lovell Telescope in England, the 64 m Sardinia Radio Telescope in Italy, the Westerbork Synthesis Radio Telescope (made up of 14, 25 m dishes) in the Netherlands, and the Nancay Radio Telescope in France, a Kraus-type design consisting of a flat primary and cylindrical secondary surface. The EPTA collaboration has categorised 18 pulsars as *Priority 1*, meaning that they offer the highest timing precision using their telescopes. They are the most promising candidates for gravitational wave detection.

⁶ <http://www.epta.eu.org/>

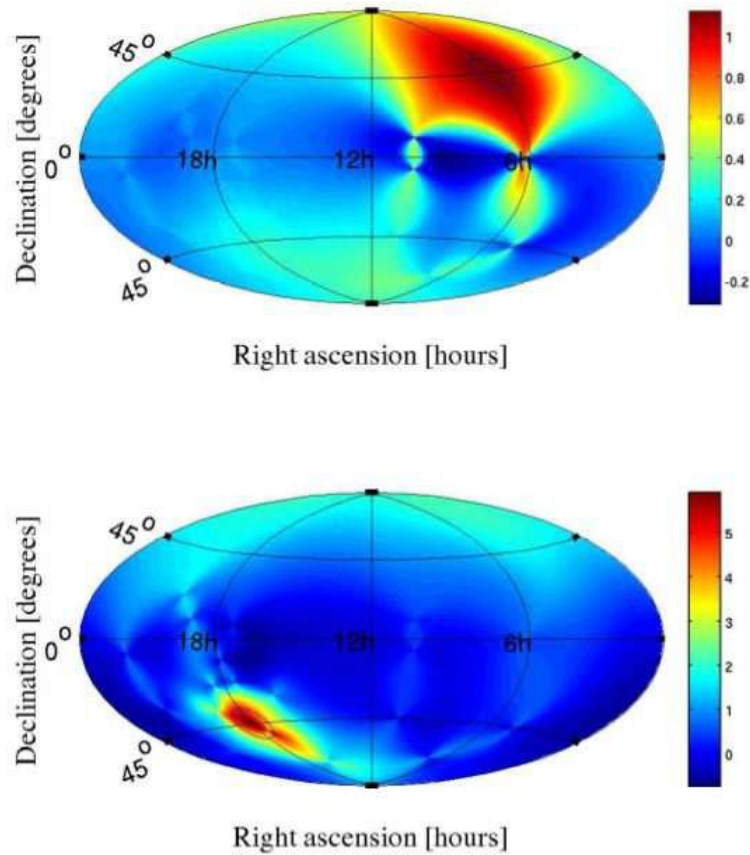


Figure 2.3: Localisation of a source of GWs in the northern sky (upper) and in the southern sky (lower) using simulated data for the pulsars observed by the PPTA. The actual assumed source positions are 06^h , 45° and 18^h , -45° . The position is better constrained for the southern hemisphere because the PPTA pulsars are more numerous in that part of the sky. Figure from Anholm et al., 2009.

- The North American Nanohertz Observatory for Gravitational Waves⁷ (NANOGrav) is a collaboration between USA and Canada. They use the 100 m Green Bank Telescope in the US and the 305 m Arecibo Observatory in Puerto Rico, to time 42 MSPs.
- The Parkes Pulsar Timing Array⁸ (PPTA) uses the 64 m Parkes Observatory in Australia.

These three collaborations also work together forming the International Pul-

⁷ <http://nanograv.org/>

⁸ <http://www.atnf.csiro.au/research/pulsar/ppta/>

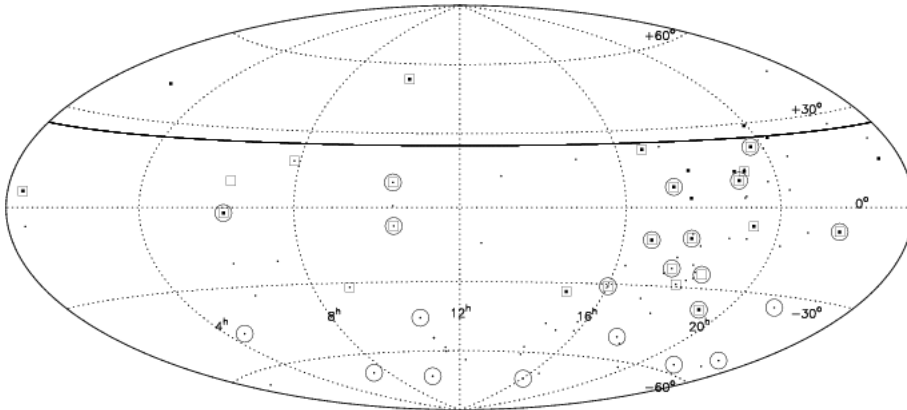


Figure 2.4: Sky-map, in equatorial coordinate system, of the pulsars included in the Parkes Pulsar Timing Array sample (large open circles), the European Pulsar Timing Array (open boxes), NANOGrav (solid boxes) and all known pulsars with $P < 20$ ms. Figure from Hobbs, 2012.

sar Timing Array⁹ (IPTA). Here, data coming from all the telescopes of the three collaborations are studied together to achieve quicker the goal of detecting GWs.

Figure 2.4 shows the distribution in the sky of the MSPs known today. We can see that most of the pulsars are found in the southern hemisphere. That is why the IPTA is important. Besides, among others, this is one of the reason why the *Square Kilometre Array* (SKA) is being built in two countries in the south hemisphere (see below paragraph 2.2.2 about SKA). A part from GW detections, PTA are used to develop a pulsar-based time standard (independent of terrestrial time standards) and to refine Solar system ephemerides. That is because errors linked to the Earth based time standard and in the models of the Solar System induce a monopolar and dipolar residual in the TOA, respectively, and so are well detectable and correctable.

2.2.2 Latest and future results

In 1974, observations of the energy loss of the binary pulsar PSR 1913+16 were attributed to the emission of gravitational waves (Taylor and Hulse, Nobel prize 1993). The observation agreed with the theoretical expectation of general relativity to better than 0.1%. That was the first proof of the existence of GW and it was due to pulsars, even though the method was different from the one explained above.

PTA is almost a newborn technique and, most of all, it is time demanding.

⁹ <http://www.ipta4gw.org/>

Therefore, results are not so high-sounding, yet. Nonetheless, data collected so far are used to:

- improve noise detection and correction: as we saw previously, the detection of a GW signal is a very precise work, where one has to delete or minimize all other noises and eventually come up with a *timing residual* of few μs over an observation of several years (e.g., see Tab.4 in Verbiest et al., 2016);
- refine pulsar and GW source models: we understood that having the best pulsar model is a fundamental starting point for these investigation. Moreover, we also want to know what to look for. For this reason modelling properly SMBBHs or any other GW source is a key step to the whole work¹⁰;
- put constrains to
 - a) Astrophysical Gravitational Wave Background (A-GWB). This GWB is the expected background of GWs emitted by all SMBBHs in the universe. See right panel of Figure 2.5 and below for further explanation;
 - b) cosmic (super)string tension. Cosmic strings are one-dimensional topological defects, relic of an early stage of the Universe, when it was more symmetric. They were created through a spontaneous mechanism of symmetry breaking, during the numerous phase transitions of the early Universe. Two cosmic strings may interact with a certain probability, and give birth to loops. Cosmic string loops oscillate and decay emitting all of their energy in various forms of radiation, with the dominant form thought to be GWs. PTA gives an upper limits on the linear energy density of this cosmic (super)string network;
 - c) Relic Gravitational Waves Background (R-GWB). Quantum fluctuations of the gravitational field in the early Universe, amplified by an inflationary phase, are expected to produce a stochastic relic GWB.

The A-GWB is particularly important because it gives information about SMBBHs and GWs with frequencies of the order of nHz. Indeed, those are the sources that I will consider for my study. For example, Lentati, 2015 show how current data set a limit on the number density of SMBHBs mergers per

¹⁰ For more on SMBBH see Chapter 3.

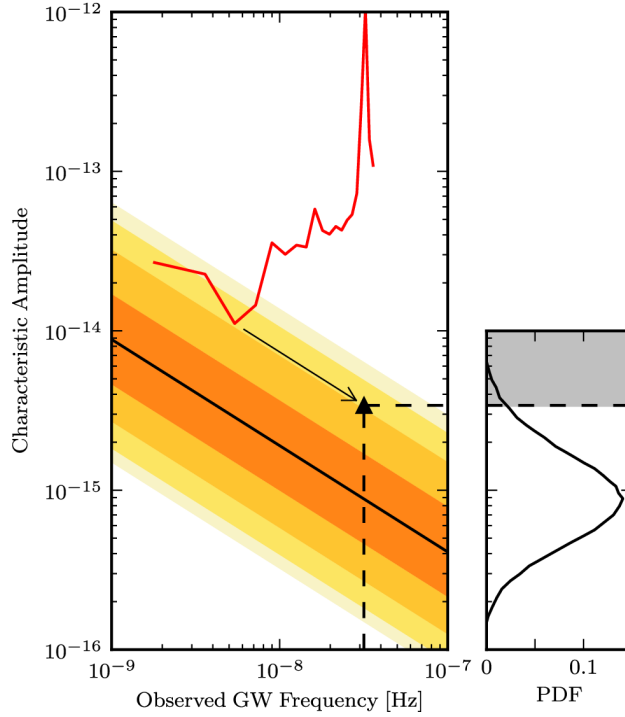


Figure 2.5: Comparison between the expected GWB amplitude from a simulated cosmological population of SMBHBs and the 95 per cent upper limit obtained with PTA experiment. Shaded areas represent the central 68, 95, 99.7 and 100 per cent confidence interval of the predicted signal according to modelling, whereas the red curve is the 95 per cent upper limit presented in the paper by Lentati, 2015.

unit redshift and unit chirp mass across cosmic history, even though this limit is still weak. As shown in Figure 2.5, the red line is the limit to the GW amplitude in the frequency range of nHz (i.e., there can not be GW with amplitudes greater than that limit), given by observation from EPTA. Shaded regions are the confidence intervals for the expected amplitude, from simulations. We can see that we still are not able to detect the expected GWB, but we are quite close to it. As mentioned before (Rosado, Sesana, and Gair, 2015), detecting a single GW is different and we can not set any limit so far to their detection.

We can say that PTA is almost at its beginning and both instruments and data processing are improving quickly. For these reasons, there is optimism about making a "real" detection, in a couple of years. A game changer in this field will be the Square Kilometre Array (SKA).

Square Kilometre Array

The Square Kilometre Array¹¹ is an international project which is building what is going to be the biggest and most sensitive radio telescope in the world. Ten countries (among which Italy and Sweden) participate in this collaboration. It is built in two phases, called SKA and SKA2. The first stage, whose building has begun in April, 2017, will work at approximately 10% of the final total power of the observatory and it should be operative in 2020. The second and final stage, SKA2, should be finished and working by the end of the 2020s. When complete, the SKA will consist of two different observatories, in Australia and in South Africa plus other countries in Africa. Each observatory will have an extended array (with thousands of antennae) of three different types of antennae distributed over a distance of more than 3000 km. This will give the SKA a sensitivity corresponding to a telescope with a square kilometre mirror, and (i) a frequency range between 50 MHz (6 m) and 14 GHz (0.02 m), (ii) the highest sensitivity for a radio telescope (more than 50 times more sensitive than the best current radio telescopes) and (iii) a wide field of view¹².

This project will help deeply the research in many different aspects. For what concerns the work of this thesis, it will increase the number of known pulsars (SKA2 potentially could detect all galactic radio emitting pulsars in the SKA sky, beaming in our direction) and study them with an unprecedented precision, as well as increasing data quality of the already known pulsars. Furthermore, with respect to Figure 2.3, it will also reduce the uncertainties in the position of the GW sources in the sky. Without any doubt, this will allow us to study GWs in depth and with a precision much higher than current PTAs (see Figure 2.1).

¹¹ www.skatelescope.org and Lazio, 2009.

¹² Shao, 2015

Chapter 3

Super Massive Binary Black Holes

In this section I present the characteristics of the GWs detected by PTAs just shown, the possible sources of these GWs, black-holes (BH), and the possible EM signal from these.

Black-holes are the most compact and relativistic object in Universe. A BH density is so dense that nothing within its Schwarzschild radius ($r_S = 2GM/c^2$) can escape it¹, not even light. From observations, we know that there exist two types of BH: stellar BH and super massive BH (SMBH). Other two types of BH, intermediate mass BH and micro BH could exist but, so far, have not observed. Micro BH are thought to be created in the very first phase of a high-dense Universe, while the nature of intermediate mass BH, which have masses between 10^2 to $10^{4-5} M_\odot$, is still questioned because, to date, there are no direct evidence of them and their birth is debated. Stellar BH is the last stage of a star with a mass above the Tolman–Oppenheimer–Volkoff (TOV) limit. Above this limit, the collapse of the star can not be stopped by its matter content and, therefore, it becomes a BH. Stellar BHs have masses of about $10 M_\odot$. Super massive BHs have masses between 10^5 and $10^{10} M_\odot$. They are believed to be present in the core of every massive galaxy². There are currently many models which explain the existence of this type of BH in the core of galaxies. The main point for my work is that their presence in the Universe is widely proved.

Super massive binary black holes (SMBBHs), then, are due mainly to galaxies mergers. Indeed, SMBHs in the core of these galaxies may create a binary system, live separately in an in-spiral phase and eventually merge together. This process is very prolonged and could lasts millions of years. A useful summary of the evolution of these kind of systems can be found in chapter 3

¹ This is true for non rotating, not charged BH, also called Schwarzschild BH.

² Kormendy and Richstone, 1995.

of Tanaka and Haiman, 2013, and I give a short summary in chapter 3.2. The number of these binary systems is unknown. There are some articles in literature, which try to verify whether or not there could be actually detectable systems. Meaning not just that they exist in the Universe, but also that there are some of them sufficiently close and/or very bright in GW signal to emerge from the background radiation. In the work by Sesana, Vecchio, and Volonteri, 2009, it is said that, depending on massive black holes population models, there should be, on average, at least one resolvable source producing a timing residual in the range of PTAs.

3.1 Characteristics of the emitted gravitational signal

Not introducing further complications, the frequency emitted by these SMBBHs can be calculated as explained above in paragraph 1.1.2, and turns out to be twice the orbital frequency. Obviously, due to this emission, the system lose energy, evolve and enters an in-spiral phase, where the main energy loss by the system is due to GWs emission. This phase terminates at the last stable orbit (LSO). The frequency (or period) at this LSO is

$$\begin{aligned} f_{LSO} &= 4.4 \cdot 10^{-6} M_9^{-1} \text{ Hz} \\ &\Downarrow \\ T_{LSO} &\approx 3 \cdot M_9 \text{ days,} \end{aligned} \tag{3.1}$$

where M_9 is the total mass of the two SMBBHs in units of $10^9 M_\odot$. Therefore, we are at the border of the PTA sensitivity for the total mass of the binary $M \approx 10^{10} M_\odot$, while for lower masses, the GWs at LSO would be not detectable for current PTAs. For the in-spiral phase, PTA will be capable of detecting GWs coming from binaries with $m_{1,2} \geq 10^8 M_\odot^3$, where $m_{1,2}$ are the masses of the SMBBHs. The changing rate of the frequency in the in-spiral phase is

$$\dot{f} = \frac{95}{6} \pi^{8/3} \mathcal{M}^{5/3} f^{11/3}, \tag{3.2}$$

where $\mathcal{M} = m_1^{3/5} m_2^{3/5} / (m_1 + m_2)^{1/5}$, is called the *chirp mass* and determines the leading order amplitude and frequency evolution of GWs. This equation will be useful later on [see eq. (3.6)], when I will talk about how this change in frequency with time could affect observations. There, I will give

³ Further details in Sesana and Vecchio, 2010

some numerical examples as well. As showed earlier, GWs induce a perturbation on space-time, $h_{\alpha\beta}(t)$. If we consider a pulsar emitting a radio pulse with frequency ν_0 , this perturbation gives birth to, for an observer at Earth, a frequency shift on the emitted frequency of the pulsar, according to the characteristic two-pulse function

$$z(t, \bar{\Omega}) \equiv \frac{\nu(t) - \nu_0}{\nu_0} = \frac{1}{2} \frac{\bar{p}^\alpha \bar{p}^\beta}{1 + \bar{p}^\alpha \bar{\Omega}_\alpha} \Delta h_{\alpha\beta}(t, \bar{\Omega}), \quad (3.3)$$

where $\nu(t)$ is the pulsar frequency received on Earth, $\bar{\Omega}$ is the unity vector parallel to the direction of the propagation of the GW, \bar{p} is the unity vector indicating the propagation direction of radio waves from the pulsar and $\Delta h_{\alpha\beta}(t) \equiv h_{\alpha\beta}(t_p, \bar{\Omega}) - h_{\alpha\beta}(t, \bar{\Omega})$ is the metric perturbation difference at the pulsar and at the observer, respectively (see Figure 3.1). The observable, as shown earlier, is the *time residual*, given by

$$r(t) = \int_0^t dt' z(t', \bar{\Omega}). \quad (3.4)$$

The frequency shift (eq. [3.3]) depends on $\Delta h_{\alpha\beta}(t)$, which exhibits the different metric perturbations at the pulsar and the Earth. Therefore, for any kind of GW, we expect to have, for every pulsar, two different terms building the timing residual. One, the Earth term, is due to GWs passing through the Earth, and the other, the pulsar term, is due to GWs at the pulsar. For a given source, the Earth term is the same for all the pulsars in the array and it depends on seven parameters. On the other hand, the pulsar term is different for every pulsar and it depends also on the distance of the pulsar from Earth, which, for the moment, is often poorly constrained. Of course, for an isotropic radiation (i.e. R-GWB and A-GWB), these two terms are the same, or the difference between them is really small. For a single source, we expect to have different frequencies coming from the pulsar term of different pulsars. This is because GWs from Earth and pulsar terms, observed at the same time, must have left the source at different times⁴ (see Figure 3.1) and we expect the emitted frequency to evolve with time [see eq. (3.2)]. This time interval is given by source-pulsar-observer relative position and the Earth-pulsar distance. Indeed, the time span between the time the metric perturbation⁵ detected through the pulsar term was emitted (T_{pt}) and the

⁴ To picture better the pulsar term, one can think that it is as, for an EM signal, we have a mirror array in the sky which reflects the light coming from sources in the Universe. These mirrors, being at distances of 1-10 kpc, would show us the sources at different ages.

⁵ I use here the word *perturbation* in reference to $\Delta h_{\alpha\beta}(t, \bar{\Omega})$ in eq. (3.3). Given the wavelength of the radiation we are taking into account here, this is a more appropriate term than just *wave*.

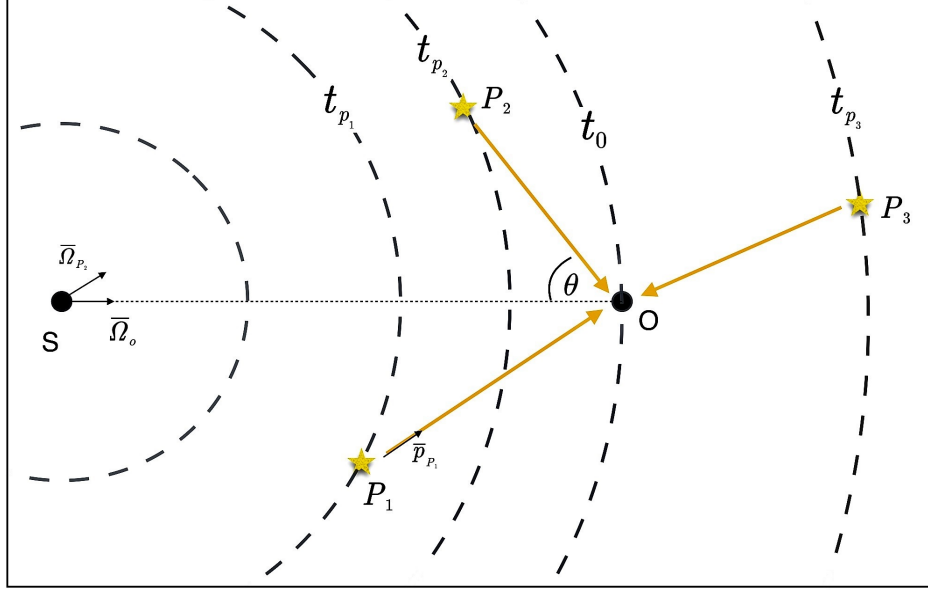


Figure 3.1: Schematic example of the system composed by a GW source, S, a PTA with three pulsars, P_1 , P_2 and P_3 , and the Earth, O. Notice that the angle between $\bar{\Omega}_o$ and $\bar{\Omega}_p$ is exaggerated in the figure. Usually it is very small because the distance pulsar-Earth ($\sim 1 - 10$ kpc) is much smaller than the distance source-Earth ($\sim 10^{2-3}$ Mpc). For more details see the text.

time the one of the earth term was emitted (T_{Et}) can be quantified as⁶

$$T_{Et} - T_{pt} = \Delta T = \frac{d}{c}(1 - \cos \theta), \quad (3.5)$$

where d is the Earth-pulsar distance, and θ is the angle between the source-Earth and the pulsar-Earth directions, see Figure 3.1. It can be shown (Sesana and Vecchio, 2010), that these two different terms should be observable and distinguishable. The change in time of the GW frequency follows from eq. (3.2) and can be further appreciated by multiplying that equation with the time interval,

$$\begin{aligned} \Delta f &= \dot{f} \Delta T = \frac{95}{6} \pi^{8/3} \mathcal{M}^{5/3} f^{11/3} \Delta T \approx \\ &\approx 0.02 \mathcal{M}_9^{5/3} f_{50}^{11/3} \Delta T \text{ nHz}, \end{aligned} \quad (3.6)$$

where $\mathcal{M}_9 = \mathcal{M}/(10^9 M_\odot)$, $f_{50} = f/(50 \text{ nHz})$ and ΔT is in year. This means that, for example, for a GW of $f = 10^{-7}$ Hz and a source with two BHs

⁶ Notice that $T_{Et} \geq T_{pt}$, i.e. T_{Et} always follows T_{pt} .

with $m_{1,2} = 10^8 M_\odot$, $\Delta f \approx 0.04$ nHz for $\Delta T = 10$ yrs. For $\Delta T = 3 \cdot 10^4$ yrs⁷, $\Delta f \approx 120$ nHz. This means that in a time interval of the order of 10 years, that is the time span of current observations, the frequency emitted can be considered constant. This is no longer true if we consider the radiation registered with the pulsar term, with respect to the Earth term.

One thing to keep in mind is that the Earth term will always be better determined because one can use all pulsars in the array to improve the S/N ratio. For this reason, we will have to wait longer, for very precise data, to work also on the pulsar terms, and that is also why, in most of current papers, the pulsar term is often ignored.

3.2 Electromagnetic signal

In order to picture what could be the EM counterparts of a SMBBH, one has to understand how the system evolves and reaches the detectable GWs emission phase. Many articles in literature try to summarize this process, among which, for example, Tanaka and Haiman, 2013 and McKernan et al., 2013 (and citations therein for further details), but they always stress the fact that there are still lots of uncertainties in modelling these stages of SMBHs mergers. This is because the complexity of the system, especially in the final detectable GWs emission phase, would take too long to be properly modelled in a 3D simulation, and therefore, most of studies use either simplified models or 1D calculations. Furthermore, observational data, as we will see later on, are still sparse.

In the process of a galaxy merger that leads to SMBBHs, stars and gas are compressed to the central region. After the first stage of star scattering, the system is compact enough for the binary to exchange momentum with the surrounding gas, and starts accelerating. The gas is expected to form a circumbinary disk (red disk in Figure 3.2). This interaction, between the binary system and the disk, aligns the two, so that they become prograde and coplanar. Then, the system is in a configuration very similar to an active galactic nucleus (AGN) and, therefore, we expect EM emission in the form of AGN. However, the central source being a binary and not a single BH, we expect some differences in the configuration of the system and, as a consequence of that, in the EM signal. In particular, there might be some time-dependent variation in the emitted radiation that will be very useful for my study.

One thing to keep in mind is that, in order to actually create a SMBBH system whose GW emission is observable via PTA, the masses of the two

⁷ I consider here a distance of pulsars of about 10 kpc and $\theta = 90^\circ$. For this distance, the value of Δf should be considered a maximum limit.

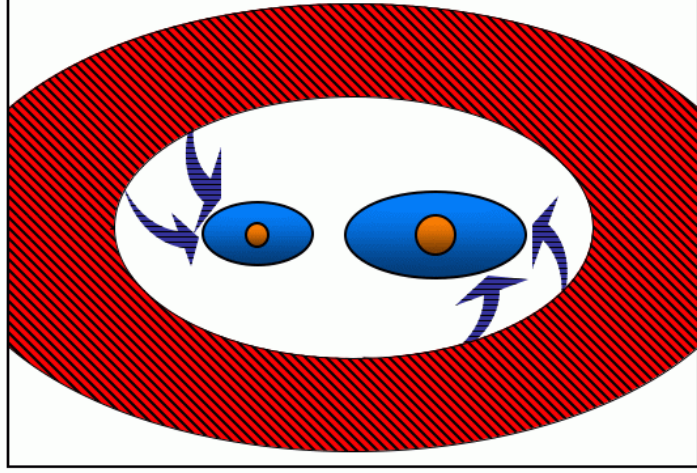


Figure 3.2: Circumbinary disk scenario in which binary torques create a low density region in the center of the disk. The accretion onto the binary members is shown by the arrows. For more details see the text. Figure from Bogdanovic et al., 2011.

SMBHs have to be comparable, i.e. $0.01 \lesssim q < 1$, where $q = m_2/m_1$ is the mass fraction with $m_2 \leq m_1$. If that is not the case, the smaller galaxy would be tidally stripped and the SMBH inside it would never reach the center of the new forming galaxy⁸. It follows that the secondary (i.e. the SMBH with lower mass) will create an annular gap about its orbital path⁹. Eventually, the gas interior to the secondary’s orbit will fall into the central SMBH and a cavity will form, as shown in Figure 3.2. As gas continues to accrete, since it cannot enter the central region and is pushed away by the binary’s tidal torque, a dam forms around the cavity (at radius $\sim 2a$, where a is the semi-major axis). If the dam is porous, as it usually seems to be, circumbinary gas leaks periodically into the cavity and could create a disk around one or both SMBHs. This is shown by the arrows and blue disks in Figure 3.2. It is still under debate how long these inner disks live. It is reasonable to think, though, that they are stable and exist until the coalescence of the BHs (e.g. see Kulkarni and Loeb, 2016). This configuration is expected to give place to particular EM signals.

i) Because the central region of an AGN is responsible for the most en-

⁸ Other articles, like Bogdanović, 2015, set the lower limit for $q \approx 0.1$. As a general rule in this chapter, given the high uncertainties on the subject, it is better always to doubt any such numerical example or constraint.

⁹ This configuration is similar to the one of a hot Jupiter opening a gap in a protoplanetary disk.

ergetic thermal photons, the presence of a cavity in that region would cut the spectrum at the highest energies and therefore it will lack of the UV and X-ray part. The peak of the SED is expected to be at lower frequencies, and it can be approximated using the equation from Tanaka and Haiman, 2013

$$\nu_{peak} \sim 10^{15} M_9^{1/4} \dot{m}^{1/4} \left(\frac{P}{1 \text{ yr}} \right)^{-1/2} \text{ Hz} \approx 3.76 \cdot 10^{14} \dot{m}^{1/4} \text{ Hz}, \quad (3.7)$$

where \dot{m} is the accretion disk rate outside the cavity in units of the critical rate corresponding to the Eddington luminosity, and the last equality is true for $M = 2 \cdot 10^9 M_\odot$ and $P = 10$ years. For Eddington ratios of 0.2 and 0.01 (the value assumed in the paper), $\nu \approx 2.5 \cdot 10^{14}$ and $1.2 \cdot 10^{14}$ Hz, respectively. The usual value for a singular SMBH is $\nu \sim 10^{16-17}$ Hz. This equation could be used, knowing ν and P from observation¹⁰, to find $\dot{m} \cdot M_{tot}$ and therefore constrain these two parameters. If we also know the total mass, then we could calculate \dot{m} , and understand the geometry of the system better. In Figure 3.3, we can see an example of a possible SED distribution.

- ii) As mentioned previously, the walls of the cavity are expected to be porous and therefore gas can fall into the cavity and create an accretion disk around one or both the SMBHs. Furthermore, these streams may shock the BHs disks and, for eccentric binaries, would give periodic flares according to the binary period or with its harmonics. Of the three unique signatures we expect from a SMBBH, this is the most difficult to model and understand. That is because many variables enter the problem, as the total mass, the ratio of the masses, the eccentricity and period of the binary system, how gas accumulate at the dam in the circumbinary disk and how it leaks in the cavity, how mini-disks form around the SMBHs and how they develop. For this reason, the subject is being studied intensely nowadays but the results are not yet always in agreement. For example, Shi and Krolik, 2016 and Farris et al., 2014 reach different conclusions about the luminosity of these flares, the former saying they are quite irrelevant, in contrast with what the latter concludes. This is why I will not use this signature further in my thesis.
- iii) The last, and most important feature, is due to Doppler effects on the emission line coming from the emitting disks, circumbinary and around

¹⁰ We will see later how we can measure P from other characteristic features.

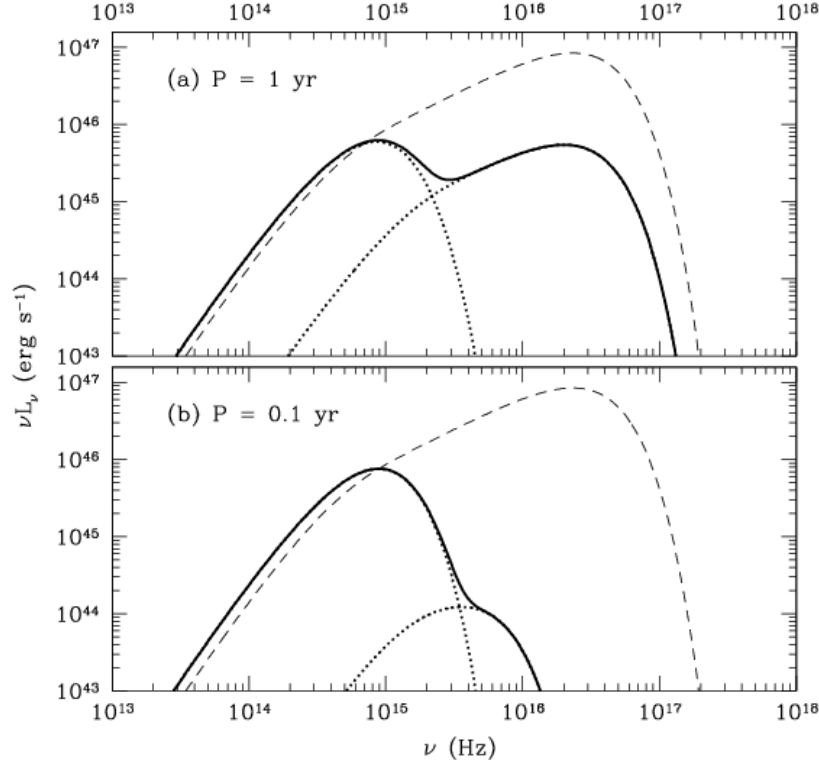


Figure 3.3: Estimated SEDs of circumbinary disks around a SMBH binary with total mass $M = 10^9 M_\odot$ and mass ratio $m_1 : m_2 = 4 : 1$. The dotted curves show the emission from the circumbinary disk truncated by a central cavity (bump at $\nu \sim 10^{15}$ Hz) and from the circumsecondary disk (higher-frequency bump). The solid curves show the composite spectrum, and the dashed curve shows, for comparison, the SED of an Eddington accretion disk around a single SMBH of the same total mass. Figure from Tanaka and Haiman, 2013.

one or both the BHs. The line we consider is the $K\alpha$ line of the Fe, because it is one of the strongest and most studied.

If there were no disks around the central BHs, the line profile would be constant with time and look like the black line on Figure 3.4. This profile depends on the emissivity characteristic of the circumbinary disk, that are listed in the paper where the figure was taken (McKernan et al., 2013). If these parameters change, then, also the line profile may change. However, if one of the BHs has an accretion disk, its Fe $K\alpha$ line profile will change with time (for any observer a part from one ob-

serving the system face-on¹¹). This change in time will depend only on the orbital period of the binary, while the flux of the line also depends on the mass ratio q , the distance between the BHs and the characteristics of the disk. In Figure 3.4, the line profile at maximum red-shift (red line) and blue-shift (blue line) are shown. The line is expected to change its shape from one to another in half the period of the binary. Therefore, from a prolonged observation, we could measure the period of the binary. In this case, though, the mass ratio is supposed to be

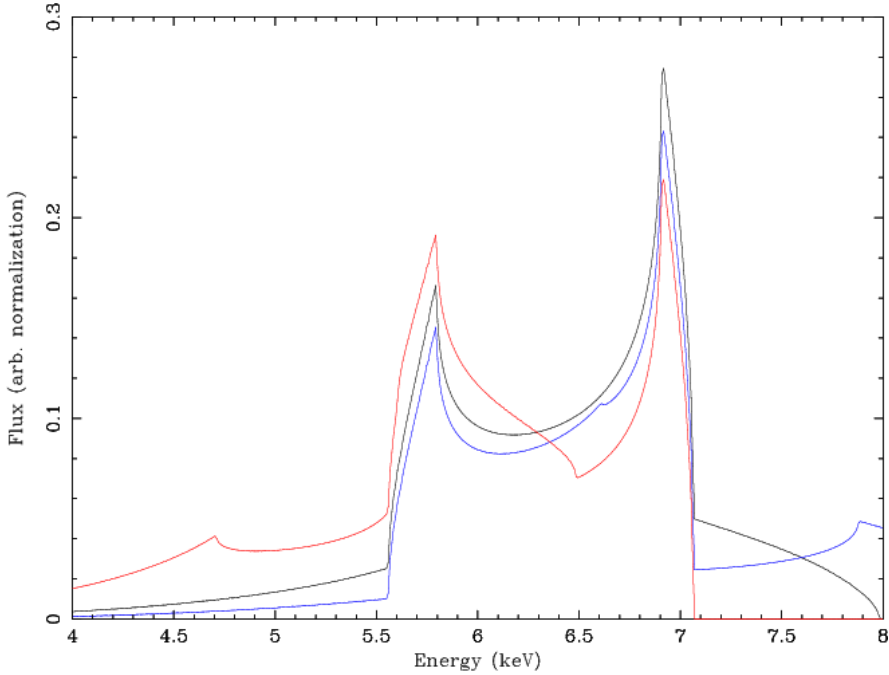


Figure 3.4: The black curve shows the Fe $K\alpha$ emission line from the circumbinary disk ($55 - 100 r_g$) plus a weak secondary broad component (10% of the intensity of the full disk profile) due to an accretion disk around the secondary black hole, located at $30 R_g$, centered on the line centroid energy (6.40 keV). The red curve shows the effect of shifting the centroid of the weak secondary component redward to 5.2 keV. The blue curve shows the effect of shifting the centroid of the weak secondary component blue-ward to 7.3 keV. The curves in both panels are binned at approximately the energy resolution (~ 7 eV) expected for *Astro-H*. Figure from Tanaka and Haiman, 2013.

rather low, $q \approx 0.01$. If the two BHs are of comparable mass, as we

¹¹ That is, for an observer who sees the velocity of the BHs along the line of sight equal to zero.

expect for binary system emitting observable GWs, there is no reason to believe only one BH to have an accretion disk. Therefore, we expect the horns of the line to "pulse" over half the orbital period, since the evolution in time of the two accretion disks is, in principle, the same but in opposition. In any case, though, whether the mass ratio is 1 or 0.01, the time-dependent configuration of the line is expected to return on its "starting" configuration after half a period. For this reason, monitoring this change in time is a powerful tool.

Figure 3.5 shows a simulation done by McKernan et al., 2013. They simulated a 350 ks (≈ 4 days) observation with *XMM-Newton* EPIC PN of an AGN at $z = 0.01$, with a 2-10 keV countrate of 3.5×10^{-11} erg/cm²/s. Simulated data are in black, and they show a Fe K α line of the secondary disk centred at 7.3 keV, that is blue-shifted. The solid blue line corresponds to the best fit to these data, while the red one is the best fit for a red-shifted line, at 5.2 keV. Data in the latter case are not presented for clarity. We can see that disentangling the circumbinary disk from the secondary disk may be difficult to realize, but repeated observation with the new generation telescopes may allow us to actually observe this feature well enough, as I will prove in the next paragraph.

3.2.1 Detectability of EM counterparts

Because of the many uncertainties and the big interest around system emitting both gravitational and EM signal, this field has been studied deeply in the last years. Many methods to study such system are being considered and modelled, and I gave a summary of the main ones¹². It is now of big importance to understand which one of these features is currently measurable and observed, and what can we expect from future observation.

The main features I am interested in for my work is the last one described in the previous chapter. Again, the detectability of this time-dependent line shape depends on many different characteristic of the system (Sesana et al., 2012), but overall there are good chances that we can observe them. Indeed, for example, Tanaka and Haiman, 2013 affirm that these oscillations should be easily detected during an extended observation with *Astro-H*¹³. In the paper by McKernan et al., 2013, it is said that even with the *XMM-Newton*

¹² But there could be others. See for example Yan et al., 2014, where they suggest to use light curves and size-wavelength relation to infer binary properties, or Kulkarni and Loeb, 2016, where they propose to use possible radio jets emission from inner disk accretion, just as a regular AGN, to understand the binary system.

¹³ The paper was written before the unsuccessful lunch of *Astro-H*. We will see later that other missions will be capable of this observations.

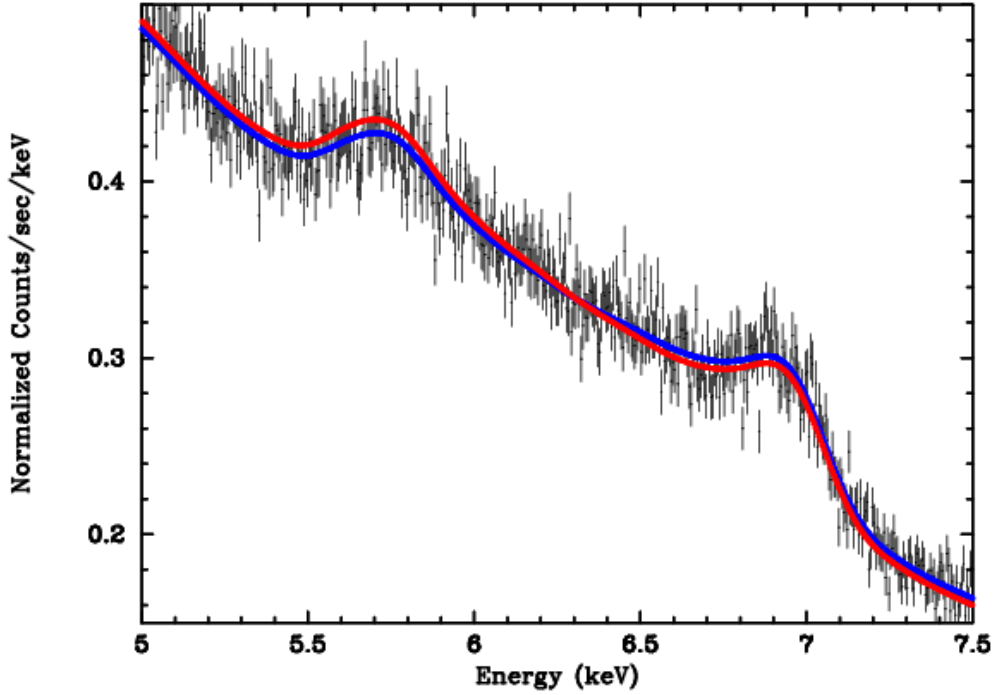


Figure 3.5: Black data points correspond to simulated data where the secondary line centroid lies at 7.3keV and the blue solid line corresponds to the best-fit model to the data. The red solid line corresponds to the best model fit when the line centroid of the secondary lies instead at 5.2keV (simulated data not shown for clarity). Further information on the text and on McKernan et al., 2013, where the figure was taken.

EPIC PN, through repeated observation, it should be possible to detect these oscillations. For a review of the main *X*-ray observatories useful for this study, see Tab. 3.1. From the table, we can see that an ideal instrument, to study the wings of the line in detail, would be one with an effective area of *LOFT* and resolution of *Athena*. Nonetheless, even with today *XMM-Newton* it should be feasible to conduct useful observations, as shown in Figure 3.5.

Both the work by Sesana et al., 2012 and McKernan and Ford, 2015 show that it will be feasible for next generation *X*-ray observatory to identify Fe $K\alpha$ features. As an example, see Figure 3.6. This is approximately the same as Figure 3.5, i.e. the AGN is at redshift $z = 0.01$ as previously, but in this case the simulated observation is done by the *Athena* observatory, the time exposure is 100 ks (≈ 1 day) and the flux is lower, $4.5 \cdot 10^{-12}$ erg cm $^{-2}$ s $^{-1}$. With respect to Figure 3.5, we can clearly see how the line shapes will be easily detected with the new generation observatory. Note that for sources

Mission	Launch	Energy range	Effective area & angular resolution	Spectral resolution
<i>XMM-Newton</i> EPIC PN ^a	10/12/1999	X-ray, IR, visible, UV	average $\approx 10^3$ cm ² ang. res. ≈ 5 arcsec	$E/\Delta E \approx 20 - 50$ at 0.15 – 15 keV
<i>MAXI</i> ^b	started working august 2009	X-ray 2 – 30 keV	$6 \cdot 10^3$ cm ² — —	$\Delta E = 135$ eV at 5.9 keV
<i>Astro-H</i> ^c	17/02/2016	X-ray 0.3 – 600 keV	300 cm ² at 30 keV ang. res. $\approx 60 - 90$ arcsec	$\Delta E \approx 7$ eV at 0.3 – 10 keV
<i>IXO/Athena</i> ^d	2028	X-ray	2 m ² at 1 keV ang. res. ≈ 5 arcsec	$\Delta E \sim 10$ eV
<i>LOFT</i> ^e	2025	X-ray 2 – 80 keV	10 m ² at 8 keV and. res. < 5 arcmin	$\Delta E < 260$ eV over the entire band

Table 3.1: Main satellite observatories.

^a X-ray Multi-Mirror-Newton European Photon Imaging Camera. <https://www.cosmos.esa.int/web/xmm-newton/home>. Spectral resolution, from the table, is $\Delta E \sim 10 - 800$ eV.

^b Monitor of All-Sky X-Ray Image, placed on the *International Space Station*. <http://cosmic.riken.go.jp/maxi/>

^c <http://astro-h.isas.jaxa.jp/en/>. Note that the 27th of march, 2016, contact was lost with the satellite and JAXA, the Japanese space agency, said it can not take control of the satellite any more. Nonetheless, it collected about one month worth of data with its instruments.

^d Advanced Telescope for High Energy Astrophysics. <http://sci.esa.int/cosmic-vision/54517-athena/>

^e Large Observatory For X-ray Timing. <http://www.isdc.unige.ch/loft/>

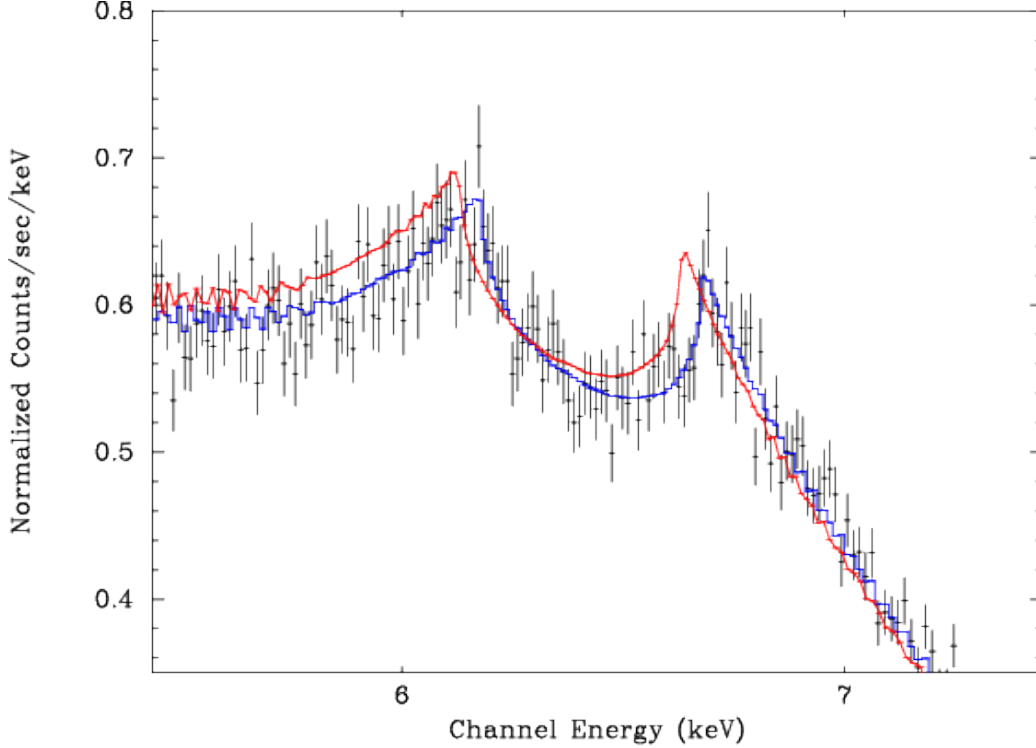


Figure 3.6: A simulated 100 ks observation with the *Athena* microcalorimeter of an AGN at $z=0.01$, with a 2–10 keV flux of $4.5 \cdot 10^{-12}$ erg cm $^{-2}$ s $^{-1}$. Black data points correspond to simulated data where the average line centroid shift is $\delta E/E = +0.004$, and the blue solid line corresponds to the best-fit model to these data. The red solid line corresponds to the best model fit when $\delta E/E = -0.004$ (simulated data not shown for clarity). Figure from McKernan and Ford, 2015.

with redshift $z = 1$, the flux is¹⁴ $\approx 4 \cdot 10^{-5}$ lower than the flux of a source with the same luminosity at $z=0.01$. This means that, to have a number of counts acceptable, we should increase the observation time of one order of magnitude, at least, i.e. 10^6 s, while in order to have the same number of counts, the integration time would be too long. To have a definitive results, though, one should run a simulation with the source at $z = 1$. For this reason, observations of sources at these distances are more complicated and it is not clear, yet, how well we could observe such features.

A special mention must be made for the Square Kilometer Array. Indeed, it will allow us to resolve individual SMBBHs emitting GWs in the PTA range

¹⁴ From $f = L/4\pi d_L^2$, where f here stays for flux, $d_L^2(z = 0.01) = (43.4)^2$ Mpc 2 and $d_L^2(z = 1) = (6701.2)^2$ Mpc 2 . I used $\Omega_M = 0.28$, $\Omega_\Lambda = 0.71$, and $H_0 = 69.6$ km/s/Mpc.

(Sesana et al., 2012) and therefore it will give us an extremely powerful tool to study these system in detail.

3.2.2 Observation

There are already some examples of real observations which suggest the presence of a binary system that I just portrayed:

- Graham et al., 2015 report the detection of a strong, smooth periodic signal in the optical variability of the quasar PG 1302-102, with a mean observed period of 1884 ± 88 days, shown in Figure 3.7. They suggest that this periodicity is due to the fact that the AGN is actually a binary system of BHs and the periodicity is given either by a preceding jet, periodic mass accretion, or a warped disk eclipsing part of the continuum as it precesses.

About the same AGN, D’Orazio et al., 2015 try to explain this periodicity stating that it is due to a lump in the circumbinary disk. That would mean that the actual period of the SMBBH is 3–8 times shorter than the 5.2 years of the optical signal variability.

This last explanation is very plausible, but has to be further proven with other observation, for example in the high energy X-ray spectrum. Until then, the uncertainties are still too large to give any definitive conclusion.

- Bon, 2016 present an analysis of 43 years (1972 to 2015) of spectroscopic observations of the Seyfert 1 galaxy NGC 5548. Observations reveal a ~ 5700 days periodicity in the continuum light curve, the $H\beta$ light curve, and the radial velocity curve of the red wing of the $H\beta$ line, see Figure 3.8. Among others explanations, they suggest that this periodicity is due to the fact that the system is a SMBBH. Also in this case, though, this hypothesis is not strong enough and can not be further proved. That is because studies on some SMBBHs models similar to this real case do not give yet details in possible emission features corresponding to the data we currently have, and models themselves could have different configurations than this case. In other cases, where Bon, 2016 tested a model, the result were not totally in agreement with data. Therefore, for the moment, other explanation are more plausible.
- Liu, Eracleous, and Halpern, 2016 looked for periodic a signal in the $H\alpha$ line for 13 possible SMBBHs system. They conclude that any periods are significantly longer than their monitoring span, and/or mechanisms other than orbiting BHs are responsible for their double-peaked broad

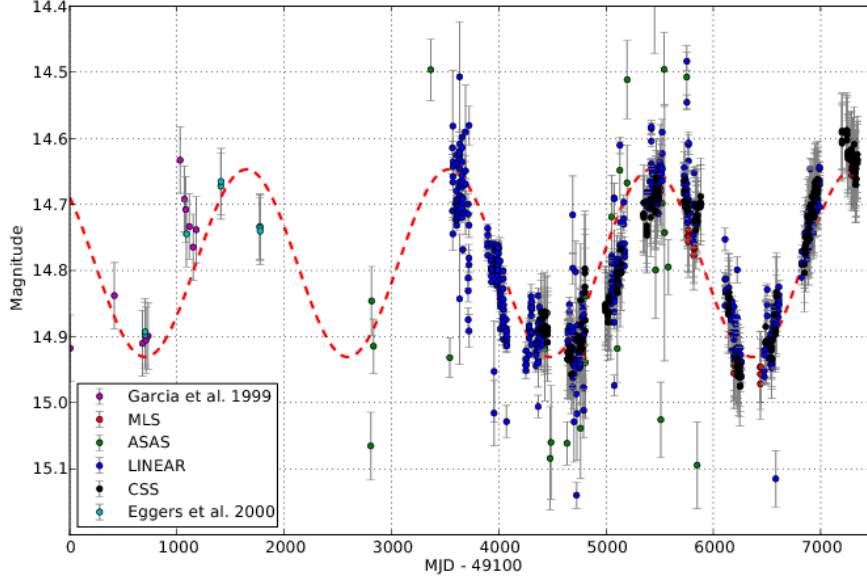


Figure 3.7: The composite light curve for PG 1302-102 over a period of 7338 days (~ 20 years). The light curve combines data from two CRTS telescopes (CSS and MLS) with historical data from the LINEAR and ASAS surveys, and the literature. The error bars represent one standard deviation errors. The dashed line indicates a sinusoid with period 1,884 days and amplitude 0.14 mag. The uncertainty in the measured period is 88 days. Note that this does not reflect the expected shape of the periodic waveform which will depend on the physical properties of the system. MJD, denotes the modified Julian day. Figure from Graham et al., 2015.

$H\alpha$ lines and their line profile changes. This, and the previous example, prove how difficult this task is and that the search for SMBBHs could be really time demanding with current technologies and data, and that not always will lead to a certain SMBBH detection. Nonetheless, their articles are a good review to better understand what to expect from a SMBBH in terms of spectral analysis.

- Kun et al., 2014 perform an analysis of long-term VLBI data of the quasar S5 1928+738 in terms of a geometric model of a helical structure projected onto the plane of the sky. The quasar is at redshift $z = 0.302$. By studying the radio jets emission data, they infer a binary with period of $T = 4.78 \pm 0.14$ yr, mass $M_{tot} = 8.13 \cdot 10^8 M_{\odot}$ and therefore a

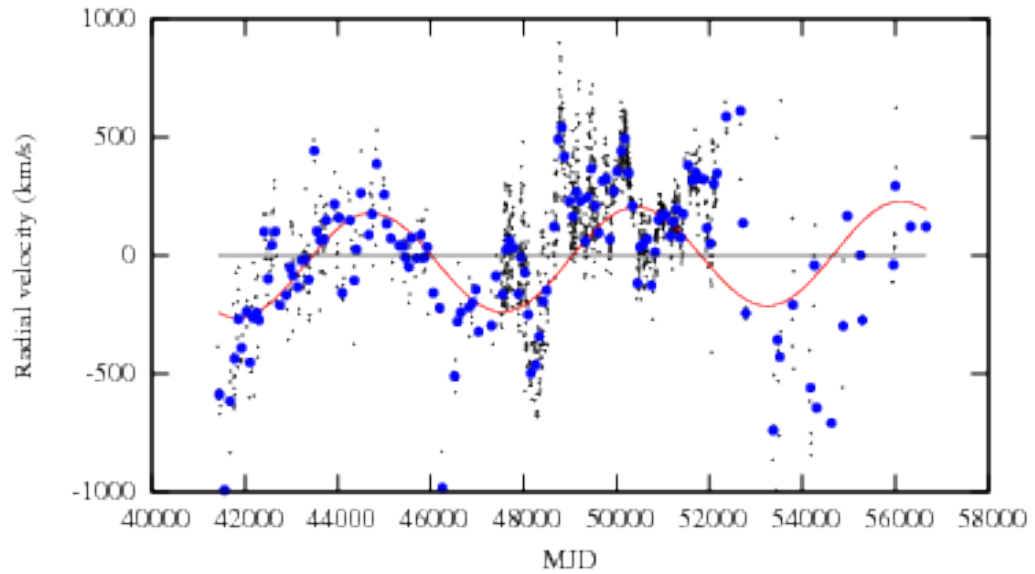


Figure 3.8: Radial velocity curves resulting from fitting a Gaussian to the broad $H\beta$ line of NGC 5548. The solid red line shows the best fit of a sine wave of period 5700 days. Figure from Bon, 2016.

separation of $R = 0.0128 \pm 0.0003$ pc. This system have parameters allowing to be resolved and observed by PTA. For this reason, this is on of the best candidate for a SMBBH system.

Chapter 4

Time delay

This chapter is the heart of my work. Here, I describe the time delay between the gravitational and EM signal, discussed previously. I will illustrate how to calculate such a time delay for the wavelengths I am interested in and constrain how well can we observe this lag nowadays and in the future. I will use all the information written above in chapter 2 and 3, including also the background set in chapter 1 and articles from literature.

4.1 Calculate time delay

In order to calculate the time delay between GWs and EM signal, we first need to understand how the waves are lensed. For the light, this is simple because we can use the geometrical optics approximation. Then, the time delay is just given by eq. (1.23). For the GWs, the calculations are less trivial, because we are in the wave optics regime. I will derive here the time delay for both *point masses* and *SIS* lenses.

4.1.1 Lensed GWs

To calculate the lensed form of GWs, $\tilde{h}_{+, \times}^L(f)$, we need to use the *amplification factor*. This is a complex function, $F(f, \beta)$, where f is the frequency of the GW¹ and β is defined in Figure 1.4, given by the diffraction integral (derived in Schneider, Ehlers, and Falco, 1992),

$$F(f, \beta) = \frac{D_d D_s (1 + z_d) f}{c D_{ds}} \int d^2\theta \exp[2\pi i f t_d(\theta, \beta)], \quad (4.1)$$

¹ For all this chapter, we consider monochromatic GWs, with frequency f .

where D_d , D_s , D_{ds} , θ and β are defined in Figure 1.4, and the time delay, $t_d(\theta, \beta)$, is defined in eq. (1.23). Then, the lensed GW is given by the product of the unlensed waveform, $\bar{h}_{+, \times}(f)$, derived in chapter 1.1, and the amplification factor, $F(f, \beta)$,

$$\tilde{h}_{+, \times}^L(f) = F(f, \beta) \cdot \bar{h}_{+, \times}(f). \quad (4.2)$$

To simplify the problem, we can consider the equation through dimensionless quantities, and rewrite them in term of the distances (D_d , D_s and D_{ds}) and of the Einstein radius, θ_E [defined in eq. (1.30)]:

$$\theta \Rightarrow x = \frac{\theta}{\theta_E}, \quad (4.3a)$$

$$\beta \Rightarrow y = \frac{\beta}{\theta_E}, \quad (4.3b)$$

$$f \Rightarrow w = \frac{D_d D_s}{c D_{ds}} \theta_E^2 (1 + z_d) 2\pi f = 8\pi \frac{GM_z}{c^3} f, \quad (4.3c)$$

$$t_d \Rightarrow T(x, y) = \frac{c D_{ds}}{D_d D_s} \theta_E^{-2} (1 + z_d)^{-1} t_d(\theta, \beta) = \frac{c^3}{4GM_z} t_d(\theta, \beta), \quad (4.3d)$$

where, in the last two equations, I substitute the value of the Einstein's radius. The amplification factor is then

$$F(w, y) = \frac{w}{2\pi i} \int d^2x \exp[iwT(x, y)]. \quad (4.4)$$

The time delay of the GW is defined from the phase of the amplification factor,

$$T_{GW}(w, y) \equiv -\frac{i}{w} \ln \left(\frac{F(w, y)}{|F(w, y)|} \right). \quad (4.5)$$

Note that this time delay, unlike the one for light, depends on the frequency of the wave.

For a *point mass* lens, the amplification factor is obtained by numerical integration (Takahashi and Nakamura, 2003),

$$F(w, y) = \exp \left[\frac{\pi w}{4} + \frac{iw}{2} \ln \left(\frac{w}{2} \right) \right] \Gamma \left(1 - \frac{iw}{2} \right) {}_1F_1 \left(\frac{iw}{2}, 1; \frac{iwy^2}{2} \right), \quad (4.6)$$

where ${}_1F_1$ is the confluent hypergeometric function (Peters, 1974). From eq. (4.5), and for $w \ll 1$, we can derive the time delay, for GWs due to a *point mass* lens, as an expansion in w ,

$$\boxed{T_{GW}(w, y) = \frac{1}{2} \left[\ln \left(\frac{w}{2} \right) + \gamma \right] + \mathcal{O}(w^2)}, \quad (4.7)$$

where $\gamma = 0.577215\dots$ is the Euler constant.

For a *singular isothermal sphere* lens, the amplification factor is obtained by numerical integration as well. The time delay, in this case, is

$$T_{GW}(w, y) = -\frac{\sqrt{\pi}}{2}w^{-1/2} - \left(1 - \frac{\pi}{4}\right) + \mathcal{O}(w^{1/2}). \quad (4.8)$$

4.1.2 Lensed light

The time delay for the EM signal is calculated in the geometrical optics regime, and it is given simply by eq. (1.23), or, in the dimensionless form, by eq. (4.3d).

For a *point mass* lens, recalling eqs. (1.27), (4.3a) and (4.3b), we obtain

$$T_{EM,\pm}(y) = \frac{y^2 + 2 \mp y\sqrt{y^2 + 4}}{4} - \ln \left| \frac{y \pm \sqrt{y^2 + 4}}{2} \right|. \quad (4.9)$$

For a *SIS* lens, we have $\theta_{\pm} = \beta \pm \theta_E$, and therefore

$$T_{EM,\pm}(y) = \mp y - \frac{1}{2}. \quad (4.10)$$

As said before, at the end of section 1.2, all these time delays can be negative since the lens potentials, ψ (defined in Tab. 1.1), are not normalized to zero at infinity. And, again, this is not a problem since we are not interested in the absolute time delay, i.e. with respect to the unlensed case, but in the difference between gravitational and EM signal arrival time.

4.1.3 Time delay

We now have all the information, summarized in Tab. 4.1, to calculate the time difference between gravitational and EM signal, defined as

$$\Delta T_{EM,\pm-GW}(x, w) = T_{EM,\pm}(y) - T_{GW}(y, w). \quad (4.11)$$

Usually, though, the arrival time difference is measured not as a time, but from the phase difference of the two waves. For this reason, what should be calculated is the (dimensionless) phase difference, given by $w\Delta T_{EM,\pm-GW}$. From this dimensionless quantity, we can obviously reconstruct the dimensional one. In particular, we can write

$$\Delta t_{EM,\pm-GW} = \frac{1}{2\pi f} w\Delta T_{EM,\pm-GW} = 0.16 \cdot w\Delta T_{EM,\pm-GW} \left(\frac{f}{\text{Hz}}\right)^{-1} \text{ sec.} \quad (4.12)$$

Lens	GW delay	EM delay	$\Delta t_{EM,\pm-GW}$
<i>Point mass</i>	$\frac{1}{2} [\ln(w/2) + \gamma] + \mathcal{O}(w^2)$	$(y^2 + 2 \mp y \sqrt{y^2 + 4})/4 + \ln (y \pm \sqrt{y^2 + 4})/2 $	$0.16 \text{ sec } (f/\text{Hz})^{-1} \cdot w \Delta T_{EM,\pm-GW}$
<i>SIS</i>	$-(w^{-1/2} \sqrt{\pi})/2 - (1 - \pi/4) + \mathcal{O}(w^{1/2})$	$\mp y - 1/2$	$0.16 \text{ sec } (f/\text{Hz})^{-1} \cdot w \Delta T_{EM,\pm-GW}$

Table 4.1: Recap of main time delays for *point mass* and *SIS* lens, depending on the source position, y , and, just for GWs, on the wave frequency, w . The values of $w \Delta T^{max}$ for different y are listed in Tab. 4.2.

For a *point mass* lens, we can calculate the maximum phase difference, for different source positions, y , (see Tab. 4.2) between the brighter EM image ($T_{EM,+}$) and the GW. For $y = 0.01$, it is $w\Delta T_{EM,+ - GW} \simeq 0.55$. Therefore, the maximum time delay, between EM and gravitational signal, is

$$\Delta t_{EM,+ - GW}^{max} = 0.09 \text{ sec} \left(\frac{f}{\text{Hz}} \right)^{-1}. \quad (4.13)$$

Therefore, for $f \approx 10^{-8}$ Hz (i.e. $T \approx 3$ yr), $\Delta t \approx 3.5$ months. For $f \approx 10^{-6}$ Hz (or $T \approx 11$ days), $\Delta t \approx 1$ day.

In the case of a *SIS* lens, for a source at $y = 0.01$,

$$\Delta t_{EM,+ - GW}^{max} = 0.1056 \text{ sec} \left(\frac{f}{\text{Hz}} \right)^{-1}. \quad (4.14)$$

In this case, for $f \approx 10^{-8}$ Hz, we get $\Delta t \approx 4$ months, that is slightly larger than before, as expected.

Note that having taken the value from Tab. 4.2, the dimensionless frequency w is fixed. Remembering its definition [eq. (4.3c)], $w \sim Mf$. For a fixed w , also the product of f and M is fixed. That is, in the first example, we would have $\Delta t \approx 3.5$ months for a lens with² $M \approx 8.3 \cdot 10^{11} M_{\odot}$, a reasonable mass for a galaxy. That is not a problem, since in a real case, if the lens mass is known, we can just insert the value in the equations. If it is not, we can use these equations to put constraints on its mass. In this last case, though, we have to possess a measure of the time delay and we need to remember that the lens mass enters also in the equation for the effective lensing potential (see Tab. 1.1) for a *point mass* lens. For a *SIS* lens, the mass does not enter in the potential equation, but we have to know the one-dimensional velocity dispersion of the stars composing the galaxy, which act as a lens.

4.2 Sensitivity of observations

I just talked about the theoretical calculations. Let us now concentrate on the observational issues. As I explained above in chapter 2, the detection of GWs, in the wavelengths range I am interested in, is a recent and evolving field. Up to now, no direct observations of GWs has been feasible with PTAs. Here, I try to estimate how good, in terms of S/N ration, the observations need to be, not just to detect GWs from a single source, but also to detect the time delay.

² From eq. (4.3c), $w = 1.1 = 1.3 \cdot f/\text{Hz} \cdot M/10^4 M_{\odot}$. Here I took a redshift for the lens of $z = 0.1$.

Lens	y	w	$w\Delta T^{max}$ (rad)	$\Delta T^{max} \cdot (f/\text{Hz})^{-1}$ (sec)
point mass	1	0.23	0.11	0.018
	0.1	0.92	0.46	0.073
	0.01	1.10	0.55	0.088
SIS	1	0.12	0.15	0.024
	0.1	1.32	0.51	0.082
	0.01	2.25	0.66	0.106

Table 4.2: Examples of maximum time delay for different source position, y , both for *point mass* and *Sis* lens. The w are obtained setting to zero the derivative of $\Delta t_{EM,+GW}(w, y)$ with respect to w , and the ΔT^{max} are obtained inserting this value of the w in the relative equations.

In the work by Cutler and Flanagan, 1994, and as reported also by Takahashi, 2016, we learn that, in a matched filtering analysis, the phase of the waveform can be roughly measured within the accuracy of the inverse signal-to-noise ratio $\approx (S/N)^{-1}$. That is, e.g. for a $S/N=10$ we can measure the phase difference if $\omega\Delta T_{EM,\pm-GW} \gtrsim 10^{-1}$ rad. Or, conversely, to detect a phase difference of³ ≈ 0.11 , we need a signal-to-noise ratio of $S/N \gtrsim (0.11)^{-1} \simeq 9.1$. Note that, both GWs and EM phases enters in $w\Delta T^{max}$. Of course, though, the observation for GWs is much more complicated than the one for the EM counterparts. For this reason, I will now concentrate on determine the signal-to-noise ratio just for GWs from PTAs detections.

The most important references, in this case, are the one by Moore, Taylor, and Gair, 2015 and Huerta et al., 2015. From Moore, Taylor, and Gair, 2015, we have

$$S/N = \varrho^2 \approx \frac{1}{2} N_p (N_p - 1) T_{obs} \int_0^T dt \frac{\chi^4 h_c^4 \sin^4(2\pi ft + \phi)}{\sigma^4 f^4 \delta t^2}, \quad (4.15)$$

where N_p is the number of pulsars in the array, T_{obs} is the total baseline time of observation, χ is the sky-averaged value of the geometric factor in eq. (3.3), $\chi = 1/\sqrt{3}$, h_c is the strain of noise fluctuations in the detector, f is the GW frequency, $\sin \phi$ is a constant offset from zero in the timing residual, σ^2 is the variance of the statistic S/N ratio, in the absence of a signal, and $1/\delta t$ is the observing cadence of the timing-residual of the pulsars.

A simpler equation is given by Huerta et al., 2015. They consider binary systems with eccentricity $e \neq 0$. Here, I derive and consider the equations in

³ I took the lowest value in Tab. 4.2.

the limit of $e = 0$. Then, we have

$$\rho_{high}^2 = \hat{\mathcal{B}} \cdot f_{orb}^{-2/3}, \text{ for } f \gtrsim \frac{2}{T_{obs}}, \quad (4.16a)$$

$$\rho_{low}^2 = \hat{\mathcal{C}} \cdot f_{orb}^{16/3}, \text{ for } f \lesssim \frac{2}{T_{obs}}, \quad (4.16b)$$

where T_{obs} is the total baseline time of observation, and therefore $T_{obs} \sim f_{obs}$, that is the lowest frequency detectable by the PTAs⁴, f_{orb} is the orbital frequency of the SMBBH (Ω in Figure 1.1), \mathcal{B} and \mathcal{C} are

$$\hat{\mathcal{B}} = \frac{4\sqrt[3]{2}\pi^{4/3}N_p(N_p - 1)T_{obs}\mathcal{M}^{10/3}(1+z)^4}{45d_L^2\Delta t\sigma_{rms}}, \quad (4.17a)$$

$$\hat{\mathcal{C}} = \frac{4\sqrt[3]{2}\pi^{4/3}N_p(N_p - 1)T_{obs}^7\mathcal{M}^{10/3}}{45d_L^2(1+z)^2\Delta t\sigma_{rms}}, \quad (4.17b)$$

where N_p is the number of pulsar in the PTA, d_L is the luminosity distance to the source, σ_{rms} is the root mean square of the timing noise, and $1/\Delta t$ is the cadence of the measurements. In order to give some numerical example, I rewrite eqs. (4.16a) and (4.17a) as⁵

$$\rho_{high}^2 = \hat{\rho}^2 \cdot (1+z)^4 \left(\frac{f_{orb}}{f_{obs}}\right)^{-2/3}, \quad (4.18)$$

with

$$\begin{aligned} \hat{\rho}^2 = & 4.26 \cdot 10^{-2} N_p(N_p - 1) \left(\frac{\mathcal{M}}{10^8 M_\odot}\right)^{10/3} \left(\frac{T_{obs}}{10 \text{ yr}}\right)^{5/3} \times \\ & \times \left(\frac{100 \text{ Mpc}}{d_L}\right)^2 \left(\frac{100 \text{ ns}}{\sigma_{rms}}\right) \left(\frac{0.05 \text{ yr}}{\Delta t}\right). \end{aligned} \quad (4.19)$$

Now, let us make some numerical calculations. First of all, as constant values through the next examples, and in Tab. 4.3, I consider sources at redshift $z = 1$, that is a luminosity distance of $d_L \simeq 6.7$ Gpc, a total observing time of $T_{obs} = 10$ yr (and therefore a $f_{obs} = 2 \cdot 3.17 \cdot 10^{-9} \text{ s}^{-1}$), an observing cadence of 1 week, i.e. $\Delta t \simeq 0.02$ yr, and a timing noise with $\sigma \approx 100$ ns. These are good approximations for current PTAs, and the sources we are looking for. The uncertainties could be in Δt , because one week is an ideal situation, and

⁴ Nonetheless, the case for $f \lesssim 2/T_{obs}$ is usually taken into account to completeness, and because SMBBHs with eccentricity $e \neq 0$ emit a spectrum of different GWs wavelengths. I will briefly talk about this case in the last chapter.

⁵ I just consider the case of $f \gtrsim 2/T_{obs}$.

$\sigma \approx 100$ ns is the lowest limit nowadays.

For a PTA with $N_p \simeq 30$ pulsars, as IPTA is, and a SMBBH with two BHs of $m_1 = m_2 = 10^8 M_\odot$, we have a signal-to-noise ratio $\rho^2 \approx 0.24$, for a $f = 2f_{orb} = 10^{-8}$ Hz, and $\rho^2 \approx 0.01$, for a $f = 2f_{orb} = 10^{-6}$ Hz. As we can understand from previous considerations, and general knowledge, this value is too low to detect the largest time delay we calculate in section 4.1.3 (see Tab. 4.2), and even to recognize just the GW signal. Therefore, with current technologies, and the assumptions made above, such an observation would be impossible. We can calculate what would be the minimum mass of the binary system, to actually detect the time delay calculated previously. I set the minimum signal-to-noise ratio at $S/N \gtrsim 5$. Then, the SMBBH has to have a mass of at least $6.3 \cdot 10^8 M_\odot$, for the time delay to be detectable up to the GW frequency of $f = 10^{-6}$ Hz. It follows, from eq. (4.18), that a higher sensitivity is necessary to detect the time delay for a smaller GW frequency. Therefore, if it is enough for $f = 10^{-6}$ Hz, it is for sure enough also for $f = 10^{-8}$ Hz, see Tab. 4.3.

Even though these observations could look feasible, as I said previously, we do not have even made any GW observations with PTA, yet, and therefore nor time delay detections. This could be due to several reasons, among which, we do not have enough precise data yet, models to study the TOA and the corrections for all the several errors (see section 2.2) are still to be improved, or also, there are no such sources or there are very few of them.

This was the case for current observatories. For the future, the SKA will improve largely on the sensitivity of the observations, i.e. reduce for example σ_{rms} , it will detect and study a lot more pulsars, and therefore will give us the opportunity to detect the time delay much more easily than today. For example, I calculated the value of the signal-to-noise ratio of an array with $N_p = 500$ pulsars, that is what we think the SKA will be capable of. I maintained all other values as before. Then, again for a SMBBH with mass of $10^8 M_\odot$, $\rho^2 \approx 3.2$ for $f = 10^{-6}$. This is still a rather low value, but much higher than the previous one. With a mass of $1.5 \cdot 10^8$, the observation could be feasible. All this numerical examples, and others, are summarised in Tab. 4.3.

frequency (s^{-1})	N_p	Mass (M_\odot)	S/N
10^{-8}	30	$1.0 \cdot 10^8$	0.24
		$2.5 \cdot 10^8$	5.3
		$3.0 \cdot 10^8$	9.3
	500	$3.5 \cdot 10^7$	1.9
		$5.0 \cdot 10^7$	6.6
		$1.0 \cdot 10^8$	70
10^{-6}	30	$1.0 \cdot 10^8$	0.01
		$6.3 \cdot 10^8$	5.2
		$8.0 \cdot 10^8$	11
	500	$5.0 \cdot 10^7$	0.3
		$1.0 \cdot 10^8$	3.2
		$1.5 \cdot 10^8$	12

Table 4.3: Examples of signal-to-noise ratios, for different masses of the SMBBHs, different number of pulsars in the PTA, and for the two limit frequencies. Note that from eq. (4.18), S/N is higher for lower frequency, when all other parameters are the same.

Chapter 5

Conclusions

In this chapter, I summarize all the thesis briefly. Then, I recap the final results of my work and discuss them. Finally, I present future works, which can be pursued taking this thesis as an initial point.

5.1 Summary

The goal of this thesis is to measure the time delay between gravitational and electromagnetic signals, due to gravitational lensing. To fulfil this goal, many different subjects were taken into account and studied. First of all, I gave the basic information about the nature of gravitational waves, i.e. what are they and how to derive their existence from general relativity. Then, I gave a simple example of a binary star system, that could be adapted to the SMBBHs case. As part of the background knowledge, I also talked about gravitational lensing, by point masses and singular isothermal sphere lenses, and stated the difference between geometrical and wave optics.

Chapter 2 was about detection of GWs. I explained how PTAs work, what are the main challenges in this field, and what are the main present result, a part from what we expect to detect in future.

After that, I focused on the sources of the signals, SMBBHs. These systems are under large investigations nowadays, and there are still many uncertainties in their creation and development and, therefore, in their signals. We know, though, that such systems have some particular features that should bring unique EM signals. There are already some observations that may be explained in this way. All this is discussed in chapter 3.

Finally, chapter 4 is the heart of this work. There, I derived how to calculate the time delay for both point masses and singular isothermal sphere lenses. Furthermore, I discuss how well GWs observation should be performed to

actually see those time delays. I gave different examples and the result of this work, that are summarised and discussed in the following chapter.

5.2 Final results & discussion

I studied the time delay between GWs and EM signals from SMBBHs. With future data from SKA, I showed that we will be able to measure the gravitational signal, coming from SMBBHs with total mass $M \gtrsim 10^8 M_\odot$, with a $S/N \approx 3$, at least. Together with observations from next generation X -ray satellites, whose sensibility needs to be further studied for distant sources, used to detect the EM counterparts, this will allow us to measure time delays of the order of months, that is a typical delay given by a galaxy, acting as a gravitational lens, of mass $M \approx 10^{11} M_\odot$.

The results obtained in this thesis are to be considered an approximation and, in some way, a simplification of the real case. Indeed, throughout this work I made a series of assumptions to simplify the numerous problems. That is because they are still under investigation, and because a deep study of the whole matter and issues is outside the scope of this thesis. Indeed, every chapter of this thesis could be a whole thesis work in itself, or even more. Nonetheless, the results are valuable and a firm starting point for future studies.

The main result is the fact that, with the next generation observatories, and with SKA in particular, we will definitively be capable of detecting the time delays between GWs and EM signal, for a large range of sources (SMBBHs composed by black-holes of $M \gtrsim 10^8 M_\odot$). The main issues of these observations is, for sure, the detection of GWs with high sensitivity. I showed that, with a number of pulsar large enough, and with constant, prolonged and precise observations, this will be possible. The precision of the detection does not depend just on the power of the observatory, but also on the exact correction of the noises and extrapolation of the signal. Furthermore, the EM counterpart will be easily detectable as well, for close sources, while for sources at redshift $z \approx 1$, it is not still clear how well this can be pursued (see chapter 3.2.1). For example, as shown in chapter 3.2, with the next X -ray satellite observatories, we will observe the unique EM signals coming from the sources. The fact that these are particular signals, expected just from binary SMBHs systems, is an advantage. Indeed, we could recognize and identify these sources easily, and we could use this feature in future surveys to find more of these systems (about this, see also chapter about future works).

Nowadays, the whole problem is a bit more complicated. According to the result of previous chapters, both GWs and EM signal from these sources are, in

theory, detectable with current technologies, even though it is very difficult. Indeed, any sign of them are yet to be found (GWs with PTAs, see chapter 2.2.2) or completely accepted and explained (EM signal, chapter 3.2.2). The effort towards a detection, though, is growing with time (just think about the IPTA), and the whole field, from GWs to SMBBHs, is being deeply researched and is of great interest nowadays. Therefore, given the result of this work, and the many studies and recent articles about this subject, I expect exiting results in the next few years.

Once we certified the theoretical feasibility of the observation, the main problem about the measurements is, to me, to couple the two different signals. That is, let us assume, as an ideal case, that we know everything about the source, the lens and we can measure the signals as precisely as we want. To prove, through observations, that the results of this thesis are valid, one should observe the signals emitted at the same time, or with a know time lag, from the source, which arrives with a certain time delay at Earth. In the real case though, the signals reaching the Earth are continuous and it could be tricky to couple two signals of different nature, arriving months one from another. The study of the evolution of the source with time could, in this case, help us. For example, if we know that at a certain point we expect some kind of different signal from the source, or if we know that to a certain EM signal corresponds a particular frequency in the gravitational signal, then we could couple the signals. Furthermore, the pulsar term, explained in 2.2, could be useful since it gives gravitational images of the sources at different times¹.

For all these reasons, the utility of this work can be seen from two different point of views:

- i. assuming that we know how to couple these two different signal, i.e. we can assert the time delay of the signals at the source, then, by studying their time delay at Earth, we can reconstruct the shape of the lens and study it in some detail;
- ii. on the contrary, if we know the characteristic of the lens, by measuring the two signals and knowing what the theoretical time delay should be, we have a powerful tool to study the source. This could be very useful, given the interest about these sources lately, and since many galaxies are expected to have or have had such a system in their center.

There could be times when both the lens and the source are unknown. In those cases, little can be done. One chance, if we are lucky enough, could be

¹ Even though being an interesting issue, I did not spend much time talking about it because its detection is very complicated, since it is different for every pulsar.

to constrain the mass of the lens by studying different EM images, and then use that information to study the delay with the gravitational waves.

5.3 Future works

As we could see throughout the whole thesis, all subjects treated comprehend a wide field of study. The first possible work would be to deepen the knowledge in all these different subjects. The main example, in this case, is the study of SMBBHs. Indeed, there are many uncertainties in this field, and a deeper study is necessary to better understand their evolution and, therefore, their emissions, both of GWs and light. This study has to be conducted mostly by computer simulations, but, to date, the problem is too complicated to make a "complete" 3D simulation and, then, simplifications have to be done. A better modelling of the EM signal could also bring other interesting information for future work. Using surveys that study all the sky, we could look for the unique signals expected from SMBBHs sources and therefore recognize them much easier than today. One of the future surveys that, among other goals, will look for these features is the *Large Synoptic Survey Telescope* (LSST)².

Another possible work could be to extend the results found here, to more general cases. For example, I considered a binary system with two BHs of the same mass, and with an eccentricity $e = 0$. Of course, in nature, we find all different cases and non zero eccentricity is believed to be the usual case for these system, because of their evolution and interaction with surrounding matter. Furthermore, SMBBHs with $e \neq 0$ are expected to emit in more than one frequency, giving birth to a spectrum, depending on their eccentricity. This could be interesting to study, since, as we saw in chapter 4.1.1, the time delay for the GWs depends on the frequency of the wave.

One last, and more difficult task, could be to study more in detail the pulsar term of the PTAs. As I explained, this could be useful since every pulsar gives a picture of the source at different epochs, depending on their distance to Earth. Since the GWs frequency change with time, this could be a powerful tool. The problem, though, is that, while for the Earth term all the signals sum up to give one single signal, for the pulsar term this is no longer the case, and the signal will be much fainter. This bring the pulsar term to be neglected and ignored nowadays. To observe and study such a feature, then, is a task for the future.

² <https://www.lsst.org/>

Appendix A

About h and GWs

I will try to explain here briefly how from

$$\bar{h}^{\alpha\beta}(t, \vec{x}) \xrightarrow{r \rightarrow \infty} \frac{4}{r} \int d^3x' [T^{\alpha\beta}(t - r, \vec{x}')]_{\text{ret}} \quad (1.13)$$

we can derive

$$\bar{h}^{ij}(t, \vec{x}) \xrightarrow{r \rightarrow \infty} \frac{2}{r} \ddot{I}^{ij}(t - r). \quad (1.14)$$

First, recall the flat-space conservation for stress-energy tensor: $\partial_\beta T^{\alpha\beta} = 0$. From this

$$\frac{\partial T^{tt}}{\partial t} + \frac{\partial T^{kt}}{\partial x^k} = 0. \quad (A.1)$$

Differentiating this equation with respect to time, and using the symmetry $T^{kl} = T^{lk}$ we find

$$\begin{aligned} \frac{\partial^2 T^{tt}}{\partial t^2} + \frac{\partial}{\partial t} \left(\frac{\partial T^{kt}}{\partial x^k} \right) &= 0, \\ \Downarrow \\ \frac{\partial^2 T^{tt}}{\partial t^2} &= - \frac{\partial}{\partial t} \left(\frac{\partial T^{kt}}{\partial x^k} \right) = - \frac{\partial}{\partial x^k} \left(\frac{\partial T^{tk}}{\partial t} \right) = + \frac{\partial^2 T^{kl}}{\partial x^k \partial x^l}. \end{aligned} \quad (A.2)$$

At this point we multiply both sides of (A.2) with $x^i x^j$ and integrate over space (i.e., over d^3x) where the right hand side is carried out by parts, to obtain:

$$\int d^3x T^{ij}(x^\mu) = \frac{1}{2} \frac{d^2}{dt^2} \int d^3x x^i x^j T^{00}(x^\mu). \quad (A.3)$$

Assuming the stress-energy tensor has no relativistic velocity (i.e. in the weak field limit) then $T^{00} \rightarrow \rho(x)$, that is the rest-mass density, we can define the quadrupole momentum:

$$I^{ij}(t) \equiv \int d^3x x^i x^j \rho(t, \vec{x}) \quad (\text{A.4})$$

and finally, substituting (A.3) and (A.4) in (1.13), we get:

$$\bar{h}^{ij}(t, \vec{x}) \xrightarrow{r \rightarrow \infty} \frac{2}{r} \ddot{I}^{ij}(t - r). \quad (1.14)$$

Bibliography

- [1] B. P. Abbott et al. “Observation of Gravitational Waves from a Binary Black Hole Merger”. In: *Phys. Rev. Lett.* 116.6 (2016), p. 061102. DOI: 10.1103/PhysRevLett.116.061102. arXiv: 1602.03837 [gr-qc].
- [2] Melissa Anholm et al. “Optimal strategies for gravitational wave stochastic background searches in pulsar timing data”. In: *Phys. Rev. D* 79 (8 2009), p. 084030. DOI: 10.1103/PhysRevD.79.084030. URL: <http://link.aps.org/doi/10.1103/PhysRevD.79.084030>.
- [3] Tamara Bogdanović. “Supermassive Black Hole Binaries: The Search Continues”. In: *Astrophys. Space Sci. Proc.* 40 (2015), pp. 103–119. DOI: 10.1007/978-3-319-10488-1_9. arXiv: 1406.5193 [astro-ph.HE].
- [4] Tamara Bogdanovic et al. “Properties of Accretion Flows Around Coalescing Supermassive Black Holes”. In: *Class. Quant. Grav.* 28 (2011), p. 094020. DOI: 10.1088/0264-9381/28/9/094020. arXiv: 1010.2496 [astro-ph.CO].
- [5] E. Bon et al. “Evidence for periodicity in 43 year-long monitoring of NGC 5548”. In: *Astrophys. J. Suppl.* 225.2 (2016), p. 29. DOI: 10.3847/0067-0049/225/2/29. arXiv: 1606.04606 [astro-ph.HE].
- [6] Sean M. Carroll. *Spacetime and geometry: An introduction to general relativity*. 2004. ISBN: 0805387323, 9780805387322. URL: <http://www.slac.stanford.edu/spires/find/books/www?cl=QC6:C37:2004>.
- [7] Curt Cutler and Eanna E. Flanagan. “Gravitational waves from merging compact binaries: How accurately can one extract the binary’s parameters from the inspiral wave form?” In: *Phys. Rev. D* 49 (1994), pp. 2658–2697. DOI: 10.1103/PhysRevD.49.2658. arXiv: gr-qc/9402014 [gr-qc].
- [8] Daniel J. D’Orazio et al. “A reduced orbital period for the supermassive black hole binary candidate in the quasar PG 1302-102?” In: *Mon. Not. Roy. Astron. Soc.* 452.3 (2015), pp. 2540–2545. DOI: 10.1093/mnras/stv1457. arXiv: 1502.03112 [astro-ph.HE].

- [9] Brian D. Farris et al. “Binary Black Hole Accretion From a Circumbinary Disk: Gas Dynamics Inside the Central Cavity”. In: *Astrophys. J.* 783 (2014), p. 134. DOI: [10.1088/0004-637X/783/2/134](https://doi.org/10.1088/0004-637X/783/2/134). arXiv: [1310.0492](https://arxiv.org/abs/1310.0492) [astro-ph.HE].
- [10] Matthew J. Graham et al. “A possible close supermassive black-hole binary in a quasar with optical periodicity”. In: *Nature* 518 (2015), p. 74. DOI: [10.1038/nature14143](https://doi.org/10.1038/nature14143). arXiv: [1501.01375](https://arxiv.org/abs/1501.01375) [astro-ph.GA].
- [11] J.B. Hartle. *Gravity: An Introduction to Einstein’s General Relativity*. Addison-Wesley, 2003. ISBN: 9780805386622. URL: <https://books.google.se/books?id=ZHgpAQAAAJ>.
- [12] R.W. Hellings and G.S. Downs. “Upper limits on the isotropic gravitational radiation background from pulsar timing analysis”. In: *apjl* 265 (Feb. 1983), pp. L39–L42. DOI: [10.1086/183954](https://doi.org/10.1086/183954).
- [13] G. Hobbs. “The Parkes Pulsar Timing Array: What we’ve done and what we’re doing”. In: *ArXiv e-prints* (Oct. 2012). arXiv: [1210.0977](https://arxiv.org/abs/1210.0977) [astro-ph.IM].
- [14] E. A. Huerta et al. “Detection of eccentric supermassive black hole binaries with pulsar timing arrays: Signal-to-noise ratio calculations”. In: *Phys. Rev. D* 92.6 (2015), p. 063010. DOI: [10.1103/PhysRevD.92.063010](https://doi.org/10.1103/PhysRevD.92.063010). arXiv: [1504.00928](https://arxiv.org/abs/1504.00928) [gr-qc].
- [15] J. Kormendy and D. Richstone. “Inward Bound—The Search For Supermassive Black Holes In Galactic Nuclei”. In: *araa* 33 (1995), p. 581. DOI: [10.1146/annurev.aa.33.090195.003053](https://doi.org/10.1146/annurev.aa.33.090195.003053).
- [16] Girish Kulkarni and Abraham Loeb. “Radio Crickets: Chirping Jets from Black Hole Binaries Entering their Gravitational Wave Inspiral”. In: *Mon. Not. Roy. Astron. Soc.* 456.4 (2016), pp. 3964–3971. DOI: [10.1093/mnras/stv2940](https://doi.org/10.1093/mnras/stv2940). arXiv: [1507.06990](https://arxiv.org/abs/1507.06990) [astro-ph.GA].
- [17] E. Kun et al. “A spinning supermassive black hole binary model consistent with VLBI observations of the S5 1928+738 jet”. In: *Mon. Not. Roy. Astron. Soc.* 445.2 (2014), pp. 1370–1382. DOI: [10.1093/mnras/stu1813](https://doi.org/10.1093/mnras/stu1813). arXiv: [1402.2644](https://arxiv.org/abs/1402.2644) [astro-ph.HE].
- [18] J. Lazio. “The Square Kilometre Array”. In: *Panoramic Radio Astronomy: Wide-field 1-2 GHz Research on Galaxy Evolution*. 2009, p. 58. arXiv: [0910.0632](https://arxiv.org/abs/0910.0632) [astro-ph.IM].
- [19] L. Lentati et al. “European Pulsar Timing Array Limits On An Isotropic Stochastic Gravitational-Wave Background”. In: *Mon. Not. Roy. Astron. Soc.* 453.3 (2015), pp. 2576–2598. DOI: [10.1093/mnras/stv1538](https://doi.org/10.1093/mnras/stv1538). arXiv: [1504.03692](https://arxiv.org/abs/1504.03692) [astro-ph.CO].

- [20] Jia Liu, Michael Eracleous, and Jules P. Halpern. “A Radial Velocity Test for Supermassive Black Hole Binaries as an Explanation for Broad, Double-peaked Emission Lines in Active Galactic Nuclei”. In: *The Astrophysical Journal* 817.1 (2016), p. 42. URL: <http://stacks.iop.org/0004-637X/817/i=1/a=42>.
- [21] Ryan S. Lynch. “Pulsar Timing Arrays”. In: *Journal of Physics: Conference Series* 610.1 (2015), p. 012017. URL: <http://stacks.iop.org/1742-6596/610/i=1/a=012017>.
- [22] R. N. Manchester. “Detection of Gravitational Waves using Pulsar Timing”. In: *ArXiv e-prints* (Apr. 2010). arXiv: 1004.3602 [astro-ph.HE].
- [23] E. Martínez Palafox et al. “Supermassive Black Hole Binaries: Environment and Galaxy Host Properties of PTA and eLISA sources”. In: *ArXiv e-prints* (Oct. 2014). arXiv: 1410.3563.
- [24] B. McKernan and K. E. S. Ford. “Detection of radial velocity shifts due to black hole binaries near merger”. In: *Mon. Not. Roy. Astron. Soc.* 452.1 (2015), pp. L1–L5. DOI: 10.1093/mnrasl/slv076. arXiv: 1505.04120 [astro-ph.HE].
- [25] B. McKernan et al. “Ripple effects & oscillations in the broad FeK α line as a probe of massive black hole mergers”. In: *Mon. Not. Roy. Astron. Soc.* 432 (2013), p. 1468. DOI: 10.1093/mnras/stt567. arXiv: 1303.7206 [astro-ph.HE].
- [26] Christopher J. Moore, Stephen R. Taylor, and Jonathan R. Gair. “Estimating the sensitivity of pulsar timing arrays”. In: *Class. Quant. Grav.* 32.5 (2015), p. 055004. DOI: 10.1088/0264-9381/32/5/055004. arXiv: 1406.5199 [astro-ph.IM].
- [27] T. T. Nakamura and S. Deguchi. “Wave Optics in Gravitational Lensing”. In: *Progress of Theoretical Physics Supplement* 133 (1999), pp. 137–153. DOI: 10.1143/PTPS.133.137.
- [28] R. Narayan and M. Bartelmann. “Lectures on Gravitational Lensing”. In: *ArXiv Astrophysics e-prints* (June 1996). eprint: astro-ph/9606001.
- [29] P. C. Peters. “Index of refraction for scalar, electromagnetic, and gravitational waves in weak gravitational fields”. In: *Phys. Rev. D* 9 (8 1974), pp. 2207–2218. DOI: 10.1103/PhysRevD.9.2207. URL: <https://link.aps.org/doi/10.1103/PhysRevD.9.2207>.
- [30] P. A. Rosado, A. Sesana, and J. Gair. “Expected properties of the first gravitational wave signal detected with pulsar timing arrays”. In: *mnras* 451 (Aug. 2015), pp. 2417–2433. DOI: 10.1093/mnras/stv1098. arXiv: 1503.04803 [astro-ph.HE].

- [31] P. Schneider, J. Ehlers, and E.E. Falco. *Gravitational Lenses*. 1992.
- [32] A. Sesana, A. Vecchio, and M. Volonteri. “Gravitational waves from resolvable massive black hole binary systems and observations with Pulsar Timing Arrays”. In: *Mon. Not. Roy. Astron. Soc.* 394 (2009), p. 2255. DOI: [10.1111/j.1365-2966.2009.14499.x](https://doi.org/10.1111/j.1365-2966.2009.14499.x). arXiv: [0809.3412](https://arxiv.org/abs/0809.3412) [astro-ph].
- [33] A. Sesana et al. “Multimessenger astronomy with pulsar timing and X-ray observations of massive black hole binaries”. In: *mnras* 420 (Feb. 2012), pp. 860–877. DOI: [10.1111/j.1365-2966.2011.20097.x](https://doi.org/10.1111/j.1365-2966.2011.20097.x). arXiv: [1107.2927](https://arxiv.org/abs/1107.2927).
- [34] Alberto Sesana and Alberto Vecchio. “Measuring the parameters of massive black hole binary systems with Pulsar Timing Array observations of gravitational waves”. In: *Phys. Rev. D* 81 (2010), p. 104008. DOI: [10.1103/PhysRevD.81.104008](https://doi.org/10.1103/PhysRevD.81.104008). arXiv: [1003.0677](https://arxiv.org/abs/1003.0677) [astro-ph.CO].
- [35] Lijing Shao et al. “Testing Gravity with Pulsars in the SKA Era”. In: *PoS AASKA14* (2015), p. 042. arXiv: [1501.00058](https://arxiv.org/abs/1501.00058) [astro-ph.HE].
- [36] Ji-Ming Shi and Julian H. Krolik. “How bright are the gaps in circumbinary disk systems?” In: *Astrophys. J.* 832.1 (2016), p. 22. DOI: [10.3847/0004-637X/832/1/22](https://doi.org/10.3847/0004-637X/832/1/22). arXiv: [1609.07110](https://arxiv.org/abs/1609.07110) [astro-ph.HE].
- [37] T. Suyama, R. Takahashi, and S. Michikoshi. “Wave propagation in a weak gravitational field and the validity of the thin lens approximation”. In: *prd* 72.4, 043001 (Aug. 2005), p. 043001. DOI: [10.1103/PhysRevD.72.043001](https://doi.org/10.1103/PhysRevD.72.043001). eprint: [astro-ph/0505023](https://arxiv.org/abs/astro-ph/0505023).
- [38] R. Takahashi and T. Nakamura. “Wave Effects in the Gravitational Lensing of Gravitational Waves from Chirping Binaries”. In: *apj* 595 (Oct. 2003), pp. 1039–1051. DOI: [10.1086/377430](https://doi.org/10.1086/377430). eprint: [astro-ph/0305055](https://arxiv.org/abs/astro-ph/0305055).
- [39] Ryuichi Takahashi. “Arrival time differences between gravitational waves and electromagnetic signals due to gravitational lensing”. In: *Astrophys. J.* 835 (2016). arXiv: [1606.00458](https://arxiv.org/abs/1606.00458) [astro-ph.CO].
- [40] Ryuichi Takahashi and Takashi Nakamura. “Wave effects in gravitational lensing of gravitational waves from chirping binaries”. In: *Astrophys. J.* 595 (2003), pp. 1039–1051. DOI: [10.1086/377430](https://doi.org/10.1086/377430). arXiv: [astro-ph/0305055](https://arxiv.org/abs/astro-ph/0305055) [astro-ph].
- [41] Takamitsu L. Tanaka and Zoltán Haiman. “Electromagnetic signatures of supermassive black hole binaries resolved by PTAs”. In: *Class. Quant. Grav.* 30 (2013), p. 224012. DOI: [10.1088/0264-9381/30/22/224012](https://doi.org/10.1088/0264-9381/30/22/224012). arXiv: [1309.2302](https://arxiv.org/abs/1309.2302) [astro-ph.CO].

- [42] J. P. W. Verbiest et al. “The International Pulsar Timing Array: First data release”. In: *mnras* 458 (May 2016), pp. 1267–1288. DOI: [10.1093/mnras/stw347](https://doi.org/10.1093/mnras/stw347). arXiv: [1602.03640](https://arxiv.org/abs/1602.03640) [astro-ph.IM].
- [43] Chang-Shuo Yan et al. “Microlensing of Sub-parsec Massive Binary Black Holes in Lensed QSOs: Light Curves and Size-Wavelength Relation”. In: *Astrophys. J.* 784 (2014), p. 100. DOI: [10.1088/0004-637X/784/2/100](https://doi.org/10.1088/0004-637X/784/2/100). arXiv: [1402.2504](https://arxiv.org/abs/1402.2504) [astro-ph.CO].